Supplementary Materials for

Quantifying hot carrier and thermal contributions in plasmonic photocatalysis

Linan Zhou, Dayne F. Swearer, Chao Zhang, Hossein Robatjazi, Hangqi Zhao, Luke Henderson, Liangliang Dong, Phillip Christopher, Emily A. Carter, Peter Nordlander,* Naomi J. Halas*

*Corresponding author. Email: nordland@rice.edu (P.N.); halas@rice.edu (N.J.H.)

This PDF file includes:

Materials and Methods
Supplementary Text
Figs. S1 to S17
Tables S1 and S2
References

Materials and methods:

Experiment and characterization

Catalyst preparation and treatment

CuRu surface alloy supported on MgO-Al$_2$O$_3$ (Cu-Ru-AR, 19.5 at% Cu& 0.5 at% Ru): 0.707 g (2.925 mmol) Cu(NO$_3$)$_2$ • 3H$_2$O (Sigma-Aldrich[®], #61194), 0.0190 g (~ 0.075 mmol) RuCl$_3$ • xH$_2$O (Acros organics, #A0324917), 2.308 g (9 mmol) Mg(NO$_3$)$_2$ • 6H$_2$O (Sigma-Aldrich[®], #63084) and 1.125 g (3 mmol) Al(NO$_3$)$_2$ • 9H$_2$O (Sigma-Aldrich[®], #237973) were dissolved in 15 mL DI water (Milli-Q[®] Advantage A10) to make the metal precursor solution. A second, basic solution was prepared by dissolving 2.544 g (24 mmol) anhydrous Na$_2$CO$_3$ (J.T.Baker[®], #3602-01) in 20 mL DI water.

10 mL of DI water was added to a 100 mL 5-neck, round-bottom flask and heated to 80 ˚C. The metal precursor solution and Na$_2$CO$_3$ solution were added simultaneously and in a dropwise fashion to the preheated water. The pH was monitored with a pH meter (Accumet[®] Portable, AP63) and kept at ~ pH = 8 by varying the speed of addition of both solutions, which was carried out over 15 minutes. The resulting solid slurry was allowed to stir at 80 ˚C for 24 hours before cooling to room temperature. The catalyst precursor was isolated by centrifuging the slurry at ~100 g and subsequently washed 4 times with DI water and dried in the air at 120 ˚C overnight.

To activate the catalyst prior to any measurements, the dry precursor was packed into the high-temperature reaction chamber (Harrick Scientific Products Inc., #HVC-VUV-5, quartz window) within a 2 mm-inner diameter stainless steel sample ring to get a thick, cylindrical sample pellet. After purging the chamber with 200 sccm (standard cubic centimeter per min, at 70 ˚F and 1 Bar) He for 10 mins to expel excess air, the precursor was annealed at 500 °C with a ramp rate of 10 ˚C /min and held for 1 h in 20 sccm He (Airgas, ultrahigh purity, 99.999%). Then, the gas was switched to 10 sccm H$_2$ (Airgas, research purity, 99.9999%) to reduce the sample at 500 ˚C for one hour. For thermocatalysis, precursor was packed into the chamber without using a sample ring to get a thin sample pellet so that the temperature of the whole sample was uniform.

Cu nanoparticles supported on MgO-Al$_2$O$_3$ (20 at% Cu): The preparation and treatment procedure was the same as above, but the metal precursor solution was prepared by dissolving 0.725 g (3 mmol) Cu(NO$_3$)$_2$ • 3H$_2$O, 2.308 g (9 mmol) Mg(NO$_3$)$_2$ • 6H$_2$O and 1.125 g (3 mmol) Al(NO$_3$)$_2$ • 9H$_2$O in 15 mL DI water.

Ru nanoparticles supported on MgO-Al$_2$O$_3$ (0.5 at% Ru): 0.0190g (0.075 mmol) RuCl$_3$ • xH$_2$O, 2.870 g (11.19 mmol) Mg(NO$_3$)$_2$ • 6H$_2$O and 1.399 g (3.73 mmol) Al(NO$_3$)$_2$ • 9H$_2$O were dissolved in 15 mL DI water to make the metal ion mixed solution. The preparation and treatment procedure was the same as for CuRu surface alloy sample.

Catalyst characterization

High resolution transmission electron microscopy (HR-TEM) was performed on a JEOL 2100 field emission gun transmission electron microscope (JEM-2100F) operated at 200 kV acceleration voltage.

High-angle annual dark-field scanning transmission electron microscopy (HAADF-STEM) was performed on a FEI Titan Themis[3] scanning transmission electron microscope equipped with both of spherical and chromatic aberration correctors.

UV-Vis diffuse reflectance spectra were measured in an Agilent Cary 5000 UV-Vis-NIR spectrometer. A Praying Mantis^{TM} diffuse reflection accessory (Harrick Scientific Products Inc., DRP-VA) was attached to the spectrometer to convert the light configuration from transmission mode to diffuse reflection mode. After precursor treatment, the high temperature reaction chamber containing reduced sample was sealed in He atmosphere and transferred to the Praying Mantis. The spectrum was collected from 400 to 800 nm with scan rate of 600 nm/min and MgO powder (Sigma-Aldrich®, #342793) was used as a white reference for collecting background spectrum.

Powder X-ray diffraction (PXRD) spectra were measured on a Rigaku D/Max Ultima II diffractometer with Cu Kα radiation (0.15418 nm). The spectrum was collected from 30˚ to 100˚ at a speed of 0.5 ˚/min. For reduced samples, they were quickly transferred to the micro sample holder of the XRD instrument and covered by Kapton® Film (SPEX SampePrep LLC, #3511) to avoid the oxidation of metal nanoparticles during measurement.

X-ray photoelectron spectroscopy (XPS) was performed on a PHI Quantera X-ray photoelectron spectrometer. The catalyst precursor was treated as described above and quickly transfer into the vacuum environment of XPS instrument. The system work function was calibration based on binding energy of C 1s (284.5 eV). Peak area of Cu $2p_{3/2}$, Ru $3p_{3/2}$, Mg 2s and Al 2p were used to quantify the surface atomic percentage of each element.

N$_2$O chemisorption experiments (*37*) were performed on a custom chemisorption setup; a micro tube furnace (Fig S7) combined with quadruple mass spectrometer (Hiden Analytical Inc., QIC-20). A 1/4'' outer diameter, 6'' length Swagelok 316L stainless steel tube (Swagelok, #SS-T4-S-035-20) was coated with a SilcoNert-1000 coating (SlicoTek® Corporation). A flexible ultra-high temperature heating tape (Omega® Engineering, #STH051-060) was wrapped on the outer surface of the tube with a K-type thermocouple (Omega® Engineering, #SCASS-032U-6) embedded. Two layers of ceramic fiber paper tape (ISA Sales & Service, LLC) and a layer of high temperature fiberglass tape with silicone adhesive (CS Hyde, #HTT-170408-36) were wrapped on the heating tap subsequently to achieve temperature isolation. The heating tape was powered by a temperature controller (Harrick Scientific Products, Inc., #ATC-024-3) through a bridge rectifier (AC to DC converter) and a DC voltage regulator (voltage upshift). The thermocouple was also connected to the temperature controller to form a feedback loop for temperature controlling.

50 mg of sample was packed into a quartz reaction tube (Frontier Laboratories, #Rx1-3541) with quartz wool (Millipore-Sigma, K93653586) packed at each end of the quartz tube to hold the sample. This quartz tube was then loaded into the stainless steel tube, which was subsequently connected into our photocatalysis setup. After annealing and reduction pre-treatments, the catalyst

was held at 500 °C under 20 sccm He for one hour to desorb H_2. The He gas was purified by passing through a Helium purifier (Sigma-Aldrich®, #27600-U) at the upstream of setup to decrease the oxygen and moisture impurity and avoid oxidation of sample before the chemisorption experiments. After cooling down the sample to 40 °C and allowing the temperature to stabilize for ~ 30 min, the gas was changed to 1% N_2O in He by mixing 0.2 sccm N_2O (Airgas, semiconductor grade, 99.999%) and 19.8 sccm He. The outgas was monitored in real time by mass spectroscopy at m/z = 44 (N_2O) and 28 (N_2+N_2O).

The way we got the N_2 formation rate is illustrated in Fig S9. N_2O gave a fragment signal at m/z=28, but since the signal ratio of m/z=28 to m/z=44 from N_2O is fixed and can be confirmed by measuring the pure N_2O flow, we extracted out the N_2 signal in chemisorption experiment by subtracting the signal at m/z=28 from the ratio of N_2O signal at m/z=44 and calibrated the result with calibration curve of N_2 in MS.

Physisorption surface area was measured on Autosorb®iQ (Quantachrome Instruments) using N_2 as the probe molecule; a molecular cross-section of 16.2 Å^2 and molecular weight of 28.013 g/mol were used in all calculations. A monolayer of adsorbed N_2 was obtained by fitting the data collected within pressure range of 0.05-0.20 P_0 (P_0=760 torr) using Brunauer–Emmett–Teller (BET) equation:

$$\frac{1}{w(\frac{P_o}{P}-1)} = \frac{c-1}{w_m c}\left(\frac{P}{P_o}\right) + \frac{1}{w_m c}$$

where w is the adsorbed gas quantity in mass unit per gram of sample (g N_2/g sample), w_m is the monolayer adsorbed gas quantity (g N_2/g sample) and c is the BET constant.

Surface area based on BET measurements was further calculated according to following formula:

$$S_{BET} = \frac{w_m}{M_{N_2}} \cdot N_A \cdot A_{N_2}$$

where S_{BET} is the surface area obtained from BET measurements (m^2/g), M_{N_2} is molecular weight of N_2 28.013 g/mol, N_A is the Avogadro constant $6.022*10^{23}$ mol^{-1} and A_{N_2} is the molecular cross-section of N_2 $16.2*10^{-20}$ m^2.

The specific surface concentration of copper can be calculated according the following formula:

$$C_{surf-Cu} = \frac{S_{BET} \cdot n}{N_A}$$

$C_{surf-Cu}$ is the specific surface concentration of copper atoms (mol Cu/g precursor), n is the surface density of copper nanoparticle $1.67*10^{19}$ atoms/m^2 (*38*)

Calibration of the custom N₂O chemisorption setup was done by comparing the chemisorption surface area of a commercial copper nanoparticle powder (Sigma-Aldrich®, #774081) measured by our custom N_2O chemisorption setup to the physisorption surface area measured by Autosorb®iQ. Since there is no support in commercial copper nanoparticle powder, the measured chemisorption surface area should be the same as the surface area measured by physisorption. 150 mg of copper nanoparticle powder was loaded into the N_2O chemisorption setup and reduced in 10 sccm H_2 at 250 ˚C for 1 h. After reduction, the powder was kept at 250 ˚C under 20 sccm helium for another hour to desorb H_2. The chemisorption experiment was then performed as described above. After the chemisorption experiment, the powder was removed and immediately used for the physisorption experiment. We used the same batch of copper nanoparticles powder for both of chemisorption and physisorption experiments as the reduction procedure may cause aggregation of the unsupported copper nanoparticles and result in surface area change compared to original sample.

Inductively coupled plasma mass spectroscopy (ICP-MS) was performed on a Perkin Elmer Nexion 300 inductively coupled plasma mass spectrometer to quantify the concentration of metallic elements (Copper & Ruthenium) in the catalyst. Certificated metal salt solutions, $Cu(NO_3)_2$ (10,000 ppm, #CGCU10) and $RuCl_3$ (1000 ppm, #CGRU1) were purchased from Inorganic™ Ventures and used to prepare external standard solutions for calibration measurements. A 1% HCl solution, which was prepared by diluting concentrated hydrochloric acid solution (Fluka® Analytical, #84415) with DI water, was used to dissolve sample and dilute all solutions. The external standard solutions were made as 1, 5, 10, 25, 50 ppm (mg/L) for Cu element and 0.05, 0.1, 0.2, 0.5 2, 5 ppm for Ru element by diluting appropriate volume of standard solution to 50 mL using volumetric flask while the volume of standard solutions were measured using pipette. The sample solutions were prepared by dissolving ~ 15 mg catalyst precursor and then diluted to 50 mL using volumetric flask. All solutions were added 50 μL internal standard solution (Sigma-Aldrich®, #CRM8029) before diluted to 50 mL. Sc and Y element were used as the internal standard for Cu and Ru measurement, respectively. Isotopes of Sc-45, Cu-63, Y-89 and Ru-102 were measured with the mass spectrometer

***In situ* surface temperatures** were recorded with a thermal camera (FLIR, A615) during the catalysis experiments. Direct illumination of the thermal camera with our light source did not cause any response to temperature, demonstrating that the illumination source has no mid-IR (2-10 μm) photons. Therefore measured temperature increase during photocatalysis result only from photothermal heating effects, rather than scattering of the illumination source. Low intensity (<1 mW/cm²) was used to avoid damaging the camera. After annealing and reduction pre-treatment, the window of the reaction chamber was changed to KBr window (International Crystal Labs Inc., 25 mm*2 mm) under helium purging, since quartz is not transparent in the mid-IR range and therefore incompatible with the thermal camera. The external optical transmission was calibrated to be 0.88, which gives the temperature of the heated chamber observed through the KBr window

the same as that measured by thermocouple in the reaction chamber. This value is reasonable as the transmission of KBr is ~ 0.9 from 250 nm to 26 μm. For photocatalysis, the hottest surface temperatures, localized to the laser beam profile, were used in Arrhenius equation to obtain the apparent activation barrier under various illumination conditions. For thermocatalysis, the surface temperatures were homogeneous and the average temperature was used in activation barrier calculations.

Catalysis experiments

Photocatalysis reactions were carried out in a fixed-bed, continuum-flow reactor (Harrick Scientific Products, Inc., #HVC-VUV-5). White light from a supercontinuum laser (Fianium, WL-SC-400-8, 400-900 nm, 4 ps, 80 MHz) was focused by an achromatic lens with a 100 mm focal length (Thorlab, AC254-100-A-ML) resulting in an ~ 2 mm diameter beam profile on the catalyst surface. The temperature of the chamber was maintained at 27 °C unless otherwise noted. The feed gas was pure NH_3 (Airgas, anhydrous purity, 99.99%), except in the ammonia-partial-pressure dependence experiments (Fig 2D). Gas flow rates were controlled with mass flow controllers (Alicat Scientific). The flow rates were optimized for different experiments based on two criteria: (i) high enough to make the conversion below 2% to achieve differential reactor conditions according the flow-rate-dependence experiment (Fig S13); (ii) as low as possible while maintaining high signal to noise ratios. All the catalytic reactions were operated under atmospheric pressure. The effluent composition was monitored by an online quadruple mass spectrometer (MS) (Hiden Analytical Inc., QIC-20) at m/e = 2 (H_2), 28 (N_2) and 17 (NH_3) in real time or an online gas chromatography (GC) (Shidmazu-2014) equipped with a pulsed discharge helium ionization detector (PDHID) and a molecular sieve 13X (MS-13X) packed column. MS can detect both of reactant (NH_3) and products (N_2&H_2) while GC can only detect products with the column we used. But GC gives better signal to noise ratios.

Reaction rates were quantified based on linear calibration curves of pure H_2 and N_2 for both MS and GC. As the conversion is controlled below 2%, the increase of total volume flow due to reaction stoichiometry (2NH_3 converted to 3H_2 and 1N_2) is negligible. The reaction rate was calculated according to the following equation:

$$r_{abs}(\mu mol \cdot s^{-1}) = \frac{\Delta p(\%) \cdot f(sccm)}{60\ (s \cdot min^{-1}) \cdot 22400 (ml \cdot mol^{-1})} \cdot 10^6 (\mu mol \cdot mol^{-1})$$

where Δp is the percentage change of a reactant or product in the flow while f is the flow rate of feeding NH_3

The specific reaction rate is calculated based on the mass of precursor:

$$r_0(\mu mol \cdot g^{-1} \cdot s^{-1}) = \frac{r_{abs}(\mu mol \cdot s^{-1})}{m_{precursor}(g)}$$

The turnover frequency (TOF) is calculated based on the following formula

$$TOF_{Ru}(h^{-1}) = \frac{r_{abs}(\mu mol \cdot s^{-1})}{n_{Ru}(\mu mol)} \cdot 3600(s \cdot h^{-1})$$

where n_{Ru} is the moles of ruthenium in the catalyst, which is obtained from ICP-MS measurement (Table S1).

Ammonia-flow-rate dependence was first performed to confirm the differential reactor conditions for photocatalysis with a Cu-Ru surface alloy catalyst. Since photocatalytic activity is limited to a smaller volume than thermocatalysis due to limit light penetration, the upper limit of conversion that satisfies differential reactor conditions for photocatalysis should be different from the general value for thermocatalysis, which is <15% for most reactions. The experiment was performed under 9.6 W/cm^2 white light illumination for different flow rate of ammonia and the effluent was monitored by MS. The result (Fig S13) indicates that conversion below 2% is needed to achieve the differential reactor conditions in our photocatalysis conditions.

Effect of loading amount of catalyst on photocatalysis was evaluated by testing the photocatalytic reaction rate under 9.6 W/cm^2 for different mass of the Cu-Ru surface alloy precursor. The flow rate of ammonia was 100 sccm and the effluent was monitored by MS. The sample pellet is generally prepared to be thicker than the penetration depth of light so that the power dependence experiment reflects the intrinsic behavior of photocatalysis. Consequently, not all of the catalyst in a thick sample pellet was active under illumination. Therefore, specific catalytic activity (catalytic reaction rate per gram catalyst) cannot be directly compared to thermocatalysis. This experiment was designed to minimize the amount of catalyst needed to absorb all the light and simplify comparison between photocatalytic and thermocatalytic results.

For intensity dependent experiments, the power of incident light was controlled by a variable neutral density filter from 50 to 300 mW, which corresponding to laser power density from 1.6 to 9.6 W/cm^2. The flow rate of NH$_3$ was 5 sccm for the intensity range between 1.6-3.2 W/cm^2 and 100 sccm for the intensity range of 4-9.6 W/cm^2. The effluent was monitored by MS.

For wavelength dependent experiments, 50 nm-bandwidth bandpass filters (Edmund, 25 mm diameter) were used to filter the light to wavelengths centered at 450, 475, 500, 525, 550, 575, 600, 650, 700 and 750 nm. The power of all testing wavelengths were tuned to be 100 mW (3.2 W/cm^2) by a variable neutral density filter. The flow rate of NH$_3$ was 5 sccm and the effluent was detected by GC.

Temperature dependence of reaction rate under various illumination conditions were carried out to explore the effect of light illumination on activation barrier. Approximately1.5 mg of Cu-Ru surface alloy precursor was used in configuration identical to that of photocatalysis experiments. Forty-five illumination conditions in a combination of five intensities (0.8-4 W/cm^2

with step of 0.8 W/cm^2) and nine wavelengths (450-600 nm with step of 25 nm and 600-700 nm with step of 50 nm) were investigated. For each chamber temperature (600-700 K with a step of 25K), the reaction rate was investigated for all illumination conditions and the surface temperatures of the sample pellet were recorded by thermal camera. The photocatalytic reaction rates were obtained by subtracting the reaction rate under both heating and illumination excitation from the thermocatalytic reaction rate at the same chamber temperature in the dark. The flow rate of NH$_3$ was set to 20 sccm and the effluent was monitored by GC.

The contour plot of apparent activation barrier under various illumination conditions (Fig 2C) was done through cubic interpolation of experimental data (Table S2) using Matlab 2016b package with the following code:

```
x=[450 475 500 525 550 575 600 650 700]; //x axis-wavelength
y=[0 0.8 1.6 2.4 3.2 4];//y axis-intensity
[X,Y]=meshgrid(x,y);//correlate x and y axis
z=[1.21 1.21 1.21 1.21 1.21 1.21 1.21 1.21 1.21;
0.99 0.94 0.88 0.84 0.78 0.88 1.10 1.13 1.15;
0.83 0.82 0.81 0.75 0.68 0.81 0.97 1.00 1.02;
0.73 0.62 0.57 0.54 0.47 0.68 0.83 0.84 0.92;
0.62 0.52 0.47 0.43 0.35 0.52 0.53 0.78 0.87;
0.48 0.42 0.39 0.35 0.27 0.46 0.48 0.66 0.79];//z axis-experimental apparent
activation barriers
row= 450:5:700;//new x axis
col= 0:0.175:4;//new y axis
[Row,Col]=meshgrid(row,col); //correlate new x and y axis
Nz=interp2(X, Y, z, Row, Col,'cubic');//new z axis through interpolation of
experimental data
surf(Row,Col,Nz);//3D plot
colormap hsv:
colorbar;
```

Ammonia-partial-pressure dependence experiments were performed to investigate the reaction mechanism and rate-determining step for both of photocatalysis at 6.4 W/cm^2 and thermocatalysis at 427 °C. The partial pressure of ammonia was tuned by adjusting the flow ratio of NH$_3$ and an inert gas (Ar and/or He) while keeping the total flow rate as 200 sccm and total pressure at 1 atm (atmospheric pressure). The minimum flow rate of NH$_3$ was 25 sccm, corresponding to 0.125 atm partial pressure, which is high enough to achieve differential conditions. For photocatalysis, as the increase of surface temperature depends on the thermal conductivity of gases, mixture of He and Ar was used to achieve the same surface temperature as that in pure NH$_3$ flow. For thermocatalysis, helium was used as the only balancing gas as the temperature of catalyst pellet was controlled by the chamber heating, barely depending on the thermal conductivity of gases. All the effluents were monitored by GC.

Thermocatalysis reactions were carried out in the same reactor, but with ~5 mg of catalyst precursor. The catalyst precursor was pack into the reactor without the sample ring to minimize sample thickness (~ 0.3 mm thickness, 6 mm diameter) to allow for homogeneous heating during

the reaction. Meunier and coworkers have demonstrated that with 3.3 mm thick sample pellet, the surface temperature measured by thermometer is lower than the effective temperature while the bottom temperature measured by thermocouple is significantly higher than the effective temperature (*39*). Temperatures from 500 K (227 ℃) to 800 K (527 ℃) with step of 50 degrees were tested. When evaluating the apparent activation barrier by fitting the reaction rate with the Arrhenius equation, we used the average surface temperatures measured by thermal camera rather than the temperature measured by the reactor thermocouple due to an inherent temperature gradient between the thermal couple and the sample pellet. The flow rate of NH_3 was 5 sccm and the effluent was detected by MS.

Simulation:
Adsorption cross section spectrum of a single copper nanoparticle
The absorption cross section of a Cu NP (Fig S12A) was calculated using Mie theory (*40*), for calculating the local temperature increase of a single Cu NP. The Cu NPs were modeled as spherical structures with 5 nm diameters, in an infinite medium of mixed MgO-Al_2O_3-air. The dielectric functions of Cu were taken from (*41*), while for the MgO-Al_2O_3-helium mixed layer we used an effective dielectric function obtained using the Maxwell-Garnett model(*42*) assuming a matrix of MgO-Al_2O_3 with spherical inclusions of helium (90% volume fraction). The fraction of helium was estimated based on the mass and volume of the reduced sample. After catalyst treatment, we took the sample pellet out from the sample ring and quickly measured its dimension (~2mm diameter* 1mm thickness) and mass (~1.1 mg). The components of a reduced sample includes Cu, MgO and Al_2O_3 and the mass fraction of each component can be estimated from the loading ratio in the catalyst precursor. The volume that each solid component occupied in the pellet can be calculated by solving the following equations:

$$V_{Cu} = \frac{\omega_{Cu}}{\omega_{Cu} + \frac{\omega_{Mg}}{M_{Mg}} \cdot M_{MgO} + \frac{\omega_{Al}}{M_{Al}} \cdot \frac{1}{2} \cdot M_{Al_2O_3}} \cdot m\rho_{Cu}^{-1}$$

$$V_{MgO} = \frac{\frac{\omega_{Mg}}{M_{Mg}} \cdot M_{MgO}}{\omega_{Cu} + \frac{\omega_{Mg}}{M_{Mg}} \cdot M_{MgO} + \frac{\omega_{Al}}{M_{Al}} \cdot \frac{1}{2} \cdot M_{Al_2O_3}} \cdot m\rho_{MgO}^{-1}$$

$$V_{Al_2O_3} = \frac{\frac{\omega_{Al}}{M_{Al}} \cdot \frac{1}{2} \cdot M_{Al_2O_3}}{\omega_{Cu} + \frac{\omega_{Mg}}{M_{Mg}} \cdot M_{MgO} + \frac{\omega_{Al}}{M_{Al}} \cdot \frac{1}{2} \cdot M_{Al_2O_3}} \cdot m\rho_{Al_2O_3}^{-1}$$

$$V_{He} = V - V_{Al_2O_3} - V_{MgO} - V_{Cu}$$

$$f_{He} = \frac{V_{He}}{V_{Al_2O_3} + V_{MgO}}$$

where ω_{Cu}, ω_{Mg} and ω_{Al} are the mass concentration of metal elements in catalyst precursor measured from ICP-MS, M_{MgO} and $M_{Al_2O_3}$ are the molar mass of MgO and Al$_2$O$_3$, ρ_{Cu}, ρ_{MgO} and $\rho_{Al_2O_3}$ are the density of Cu, MgO and Al$_2$O$_3$, m and V are the mass and volume of reduced sample.

Upper limit of local temperature increase of a single copper nanoparticle over the environment

Under continuum light illumination, what the IR camera measures is the steady-state ensemble temperature averaged over a timescale concomitant with the time resolution of IR camera (~ 40 ms). Because we used a pulsed laser, within several picoseconds directly after each pulse, the local temperature of each Cu NP will be higher than its environmental temperature, before heat energy was dissipated through phonon-phonon interaction (ps scale) and the local temperature of each Cu NP reached equilibrium with its environment before the next pulse (12.5 ns). We estimated that the maximum temperature increase of a single Cu NP could be above the environmental temperature when illuminated with the laser following the theory developed in Reference (*43*). In particular, we assumed that the electron-phonon thermalization occurs much faster than the heat diffusion into the environment and the time separation between laser pulses, which in our case was $\sim 1/80$ MHz ~ 12.5 ns (adiabatic assumption). This allowed us to write the maximum transient temperature increase in a single particle over the environment as

$$\Delta T_{max} = \frac{\sigma_{abs}}{V_{Cu} \cdot \rho_{Cu} \cdot c_{Cu}} \cdot \frac{I}{f},$$

being σ_{abs} the absorption cross-section of the single nanoparticle, V_{Cu} the volume of the Cu core, ρ_{Cu} the copper mass density, c_{Cu} the Cu heat capacity, I the laser intensity, and f the pulse repetition rate. This expression implies that all the energy is absorbed in the Cu core, which is a realistic assumption given the negligible absorption of Al$_2$O$_3$ and MgO in the spectral range under consideration.

As Fig. S12B shows, the instantaneous local temperature increase of Cu NPs over their environment directly following a pulsed excitation is quite small, thus the temperature increase measured by the IR camera is accurate enough to describe the photothermal heating effect in our experiment.

Supplementary Text

Size, surface structure and LSPR of photocatalysts

The particle size distribution of Cu-Ru-AR and Cu nanoparticles were similar, with an average diameter of ~5 nm (Fig. S1, S2). Ru nanoparticles synthesized under similar conditions were larger, with an average diameter of ~15 nm (Fig. S3). The surface structure of the Cu-Ru-AR was verified using N_2O chemisorption ($2Cu_s + N_2O \rightarrow Cu_2O + N_2$, where Cu_s refers to surface copper atoms) (Fig. S8). The concentration of Cu_s in the pure Cu nanoparticles is 94.8 μmol/g. In contrast, the concentration of Cu_s in the Cu-Ru-AR was measured to be 49.2 μmol/g. The decrease in concentration of surface copper (43.6 μmol/g) is close to the bulk concentration of Ru (56.5 μmol/g) in the Cu-Ru surface alloy (Table S1), suggesting that most of the Ru atoms occupy surface sites in the Cu-Ru surface alloy. UV-vis diffuse reflectance spectroscopy shows that Cu-Ru surface alloy exhibits a LSPR peak centered at ~550 nm with high absorption, nearly identical to pure Cu nanoparticles (Fig. S4).

Rationale for using surface temperature to evaluate the activation barrier

Dissociation of NH_3 on the Ru surface occurs through a precursor-mediated mechanism (*44*), where adsorbates (NH_3^{abs}) relax through rotation and diffusion to achieve an appropriate configuration at active sites, and the absorbed molecules reach thermal equilibrium with the catalyst surface before the reaction starts. The RDS, which is also the step activated by hot carriers, is N_2 desorption. The N intermediates will definitely be in thermal equilibrium with the surface after several steps of N-H bond breaking, which are mostly thermally activated. Therefore the surface temperature is the right temperature affecting the reaction kinetics in both thermocatalysis and photocatalysis.

All temperatures used in our Arrhenius equation-based analysis were the surface temperature of the catalyst measured by the IR camera, including the thermocatalysis. The catalyst pellet is thin (~0.3 mm) and thus the temperature of the whole catalyst pellet in thermocatalysis is homogeneous and the same as the surface temperature, but different from the chamber temperature measured by a thermocouple in the chamber, since there is a several-mm gap between the thermocouple and the bottom of the catalyst pellet due to the design of the commercial chamber (*39*). For photocatalysis, because the light penetration depth in the photocatalyst pellet is of the order of 10 μm (*17*), most of the light absorption, and the subsequent photo-activated reaction, happen at the thin top layer of the photocatalyst pellet. The photocatalytic reaction rates were obtained by subtracting the reaction rate at a specific illumination condition and chamber temperature from the reaction rate at the same chamber temperature in the dark. This only includes the hot-carrier-driven contribution and the photothermal effect. As we have demonstrated, the photothermal effect is very weak in the photocatalysis of this system (Fig 1D), so the above obtained photocatalytic reaction rates are dominated by the hot-carrier-driven reaction rate, and is related to the surface temperature measured by the IR camera.

Calculation of energy efficiency and quantum yield:

Ammonia decomposition reaction is an endothermic reaction with reaction enthalpy, $\Delta H^o_{rxn} = +46\ kJ/mol$. The energy efficiency (light-to-chemically stored energy conversion) was calculated as follows:

$$\eta_{energy} = \frac{reaction\ rate\ (mol\ NH_3/s) * reaction\ enthalpy\ (\frac{J}{mol\ NH_3})}{optical\ power\ (J/s)} \cdot 100\%$$

For quantum yield, since we proposed that the associative desorption of N_2 is the key elementary step activated by hot carriers, we calculate the quantum yield based on the number of generated N_2 per absorbed photon as follows:

$$Quantum\ yield = \frac{reaction\ rate\ (mol\ N_2/s) * N_A}{optical\ power\ (J/s) \Big/ \bar{E}_{photon}(J)} \cdot 100\%$$

where the N_A is the Avogadro constant and $\bar{E}_{photon}$ is the average photon energy of our light source, which is $2.83 \cdot 10^{-19}\ J$, equivalent to 1.77 eV or 700 nm.

Determination of intrinsic barrier from the measured barrier based on ambient temperature:

In the present study, $E_a(\lambda, I)$ is determined by measuring the actual surface temperature of the catalyst during the reaction, making it possible to clearly distinguish hot carrier contributions from the photothermal effect. In a situation where the temperature change of the catalyst cannot be determined independently or through calculations, the measured light dependence of the activation barrier will also include contributions from photothermal heating. For moderate light intensities I, the actual temperature T of the catalyst can be written $T = T^A + \beta I$, where T^A is the ambient temperature and the photothermal conversion $\beta(\lambda)$ will depend on the wavelength λ. The measured thermal barrier E_a^M will then be related to the intrinsic light-dependent barrier (assuming that the Arrhenius prefactors are only weakly dependent on temperature) as:

$$E_a^M(\lambda, I) = E_a(\lambda, I) \cdot \left(1 + \frac{\beta(\lambda)}{T^A} I\right)^{-1}.$$

For a fixed, low light intensity, $\beta(\lambda)$ can be determined by measuring the barrier for a few different ambient temperatures. Using this $\beta(\lambda)$, one can then extract the light-dependent activation barrier $E_a(\lambda, I)$ from the measured $E_a^M(\lambda, I)$.

Degree of Rate Control (DRC) analysis

DRC analysis (*30*) is a convenient approach for quantifying how the relative increase of the net reaction rate depends on per (differential) decrease of the standard-state free energy (G_i^0) of any species (intermediates, transition states, reactants and products). A general conclusion from DRC analysis is that the DRC of the transition state at RDS is 1 while the DRC of absorbed intermediates is a negative number with magnitude proportional to its coverage.

We propose the following reaction mechanism for the NH_3 decomposition reaction:

$$NH_3\,(g) + * \leftrightarrow NH_3^{ads} \quad (1)$$
$$NH_3^{ads} + * \leftrightarrow NH_2^{ads} + H^{ads} \quad (2)$$
$$NH_2^{ads} + * \leftrightarrow NH^{ads} + H^{ads} \quad (3)$$
$$NH^{ads} + * \leftrightarrow N^{ads} + H^{ads} \quad (4)$$
$$N^{ads} + N^{ads} \rightarrow N_2\,(g) + 2* \quad (5) \quad (RDS)$$
$$H^{ads} + H^{ads} \leftrightarrow H_2\,(g) + 2* \quad (6)$$
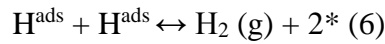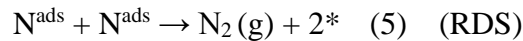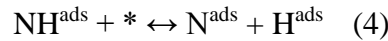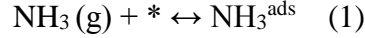
the * denotes empty sites and the superscript ads denotes a surface-adsorbed intermediate.

We applied the quasi-equilibrium approximation on the reaction steps other than the RDS and obtained the following equilibrium expressions:

$$k_1 P_{NH_3}[*] = k_{-1}[NH_3^{ads}] \rightarrow [NH_3^{ads}] = K_1 P_{NH_3}[*] \quad (7)$$
$$k_2[NH_3^{ads}][*] = k_{-2}[NH_2^{ads}][H^{ads}] \rightarrow [NH_2^{ads}] = K_2[NH_3^{ads}][*]/[H^{ads}] \quad (8)$$
$$k_3[NH_2^{ads}][*] = k_{-3}[NH^{ads}][H^{ads}] \rightarrow [NH^{ads}] = K_3[NH_2^{ads}][*]/[H^{ads}] \quad (9)$$
$$k_4[NH^{ads}][*] = k_{-4}[N^{ads}][H^{ads}] \rightarrow [N^{ads}] = K_4[NH^{ads}][*]/[H^{ads}] \quad (10)$$
$$k_6[H^{ads}]^2 = k_{-6}[*]^2 P_{H_2} \rightarrow [H^{ads}] = \left(\frac{P_{H_2}}{K_6}\right)^{1/2}[*] \quad (11)$$

k_i and k_{-i} represent the forward and back reaction rate of step i and K_i denotes the equilibrium constant of step i. P_i is the partial pressure of gaseous species i.

It is reasonable to assume that the RDS is irreversible for this reaction, since the conversion is low and the dissociative adsorption N_2 is highly activated. Thus the net reaction rate is:

$$r_{rxn} = r_5 = k_5[N^{ads}]^2 \quad (12)$$

We further derived the expression of $[N^{ads}]$ from (7)-(11) as:

$$[N^{ads}] = K_1 K_2 K_3 K_4 K_6^{3/2} \frac{P_{NH_3}}{P_{H_2}^{3/2}}[*] \quad (13)$$

Then we solved the [*] from site balance $[*] + [NH_3^{ads}] + [NH_2^{ads}] + [NH^{ads}] + [N^{ads}] + [H^{ads}] = 1$, together with expressions (7)-(11):

$$[*] = 1/\left(1 + \left(\frac{P_{H_2}}{K_6}\right)^{\frac{1}{2}} + K_1 K_2 K_3 K_4 K_6^{\frac{3}{2}} \frac{P_{NH_3}}{P_{H_2}^{\frac{3}{2}}} + K_1 K_2 K_3 K_6 \frac{P_{NH_3}}{P_{H_2}} + K_1 K_2 K_6^{\frac{1}{2}} \frac{P_{NH_3}}{P_{H_2}^{\frac{1}{2}}} + K_1 P_{NH_3}\right) \quad (14)$$

Inserting (13) and (14) into (12), we have:

$$r_{rxn} = k_5 (K_1 K_2 K_3 K_4 K_6^{\frac{3}{2}} \frac{P_{NH_3}}{P_{H_2}^{\frac{3}{2}}} / (1 + \left(\frac{P_{H_2}}{K_6}\right)^{\frac{1}{2}} + K_1 K_2 K_3 K_4 K_6^{\frac{3}{2}} \frac{P_{NH_3}}{P_{H_2}^{\frac{3}{2}}} + K_1 K_2 K_3 K_6 \frac{P_{NH_3}}{P_{H_2}} +$$

$$K_1 K_2 K_6^{\frac{1}{2}} \frac{P_{NH_3}}{P_{H_2}^{\frac{1}{2}}} + K_1 P_{NH_3}))^2 \quad (15)$$

We performed the analysis of DRC according to Ref (34):

$$k_i = (k_B T/h) \exp(-\Delta G_i^{0,TS}/RT) = (k_B T/h) \exp(-(G_{i,TS}^0 - G_{react}^0)/RT) \quad (16)$$

$$K_i = \exp(-\Delta G_i^{0,rxn}/RT) = \exp(-(G_{prod}^0 - G_{react}^0)/RT) \quad (17)$$

$\Delta G_i^{0,TS}$ is the standard-state free energy of activation for step i , $\Delta G_i^{0,rxn}$ is the standard-state reaction free energy change of step i. $G_{i,TS}^0$, G_{react}^0 and G_{prod}^0 are the standard-state free energies of transition state, reactants and products at step i, respectively.

Inserting (16) and (17) into (15), we obtain:

$$r_{rxn} = (k_B T/h) \exp(\frac{-G_{5,TS}^0 - 2\Delta G_{rxn}^0 + G_{N_2(g)}^0 + 2G_*^0}{RT}) \frac{P_{NH_3}^2}{P_{H_2}^3} /$$

$$(1 + \left(\frac{P_{H_2}}{\exp(\frac{-G_{H_2(g)}^0 - 2G_*^0 + 2G_{H^{abs}}^0}{RT})}\right)^{\frac{1}{2}} + \exp(\frac{-G_{N^{abs}}^0 - \frac{3G_{H_2(g)}^0}{2} + G_{NH_3(g)}^0 + G_*^0}{RT}) \frac{P_{NH_3}}{P_{H_2}^{\frac{3}{2}}}$$

$$+ \exp(\frac{-G_{NH^{abs}}^0 - G_{H_2(g)}^0 + G_{NH_3(g)}^0 + G_*^0}{RT}) \frac{P_{NH_3}}{P_{H_2}}$$

$$+ \exp(\frac{-G_{NH_2^{abs}}^0 - \frac{G_{H_2(g)}^0}{2} + G_{NH_3(g)}^0 + G_*^0}{RT}) \frac{P_{NH_3}}{P_{H_2}^{\frac{1}{2}}}$$

$$+ \exp(\frac{-G_{NH_3^{abs}}^0 + G_{NH_3(g)}^0 + G_*^0}{RT}) P_{NH_3})^2$$

ΔG_{rxn}^0 is the standard-state reaction free energy change of the net reaction

Set the denominator of the above formula as Z, and according to $DRC_x = \left(\frac{-\partial \ln r_{rxn}}{\partial \left(\frac{G_x^0}{RT}\right)}\right)_{G_{y \neq x}^0}$, we

have

$$DRC_{N^{ads}} = -\frac{2 \exp\left(\frac{-G_{N^{abs}}^0 - \frac{3G_{H_2(g)}^0}{2} + G_{NH_3(g)}^0 + G_*^0}{RT}\right) \frac{P_{NH_3}}{P_{H_2}^{\frac{3}{2}}}}{Z}$$

Our DRC analysis of the N intermediate (N^{ads}) results in a large negative number, especially for low conversion condition (high $\frac{P_{NH_3}}{P_{H_2}^{\frac{3}{2}}}$). Thus by destabilizing the N^{ads} through hot carrier activation, light excitation can enhance the reaction rate. It is important to note that here the DRC was used to analyze a rate law where the rate limiting step was predetermined, rather than without defining a rate limiting step, as typically done. This was simply to illustrate that when N_2 desorption is the rate limiting step, as suggested through the kinetic analysis in the main text, activation or weakening of the catalyst-N bond would facilitate the overall reaction rate.

Supplementary Figures:
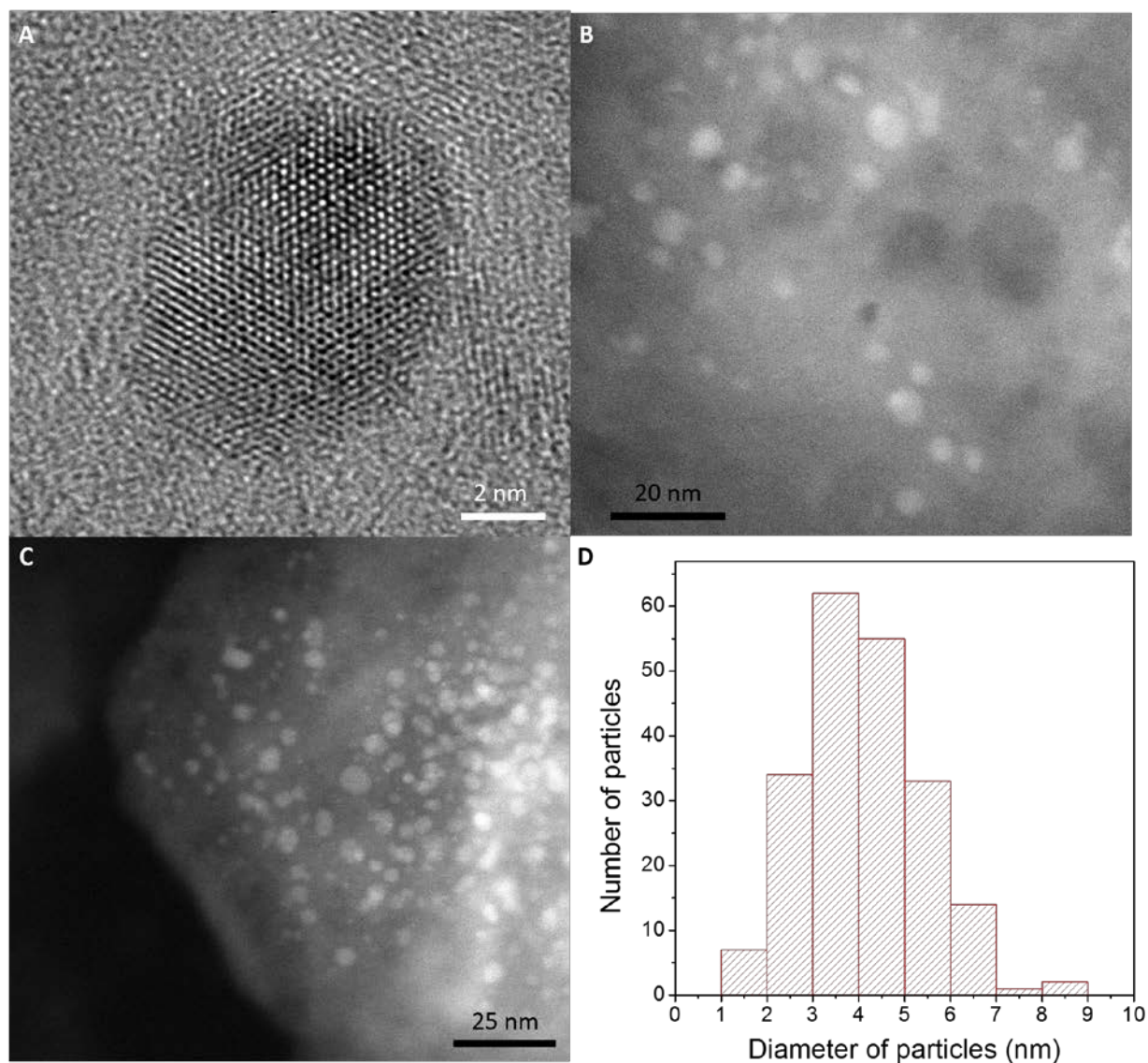
Fig. S1. (A) High-resolution transmission electron micrograph of a single Cu-Ru surface alloy. (B, C) HAADF images of reduced Cu-Ru surface alloy on MgO-Al$_2$O$_3$ support. (D) Size distribution of Cu-Ru surface alloy.
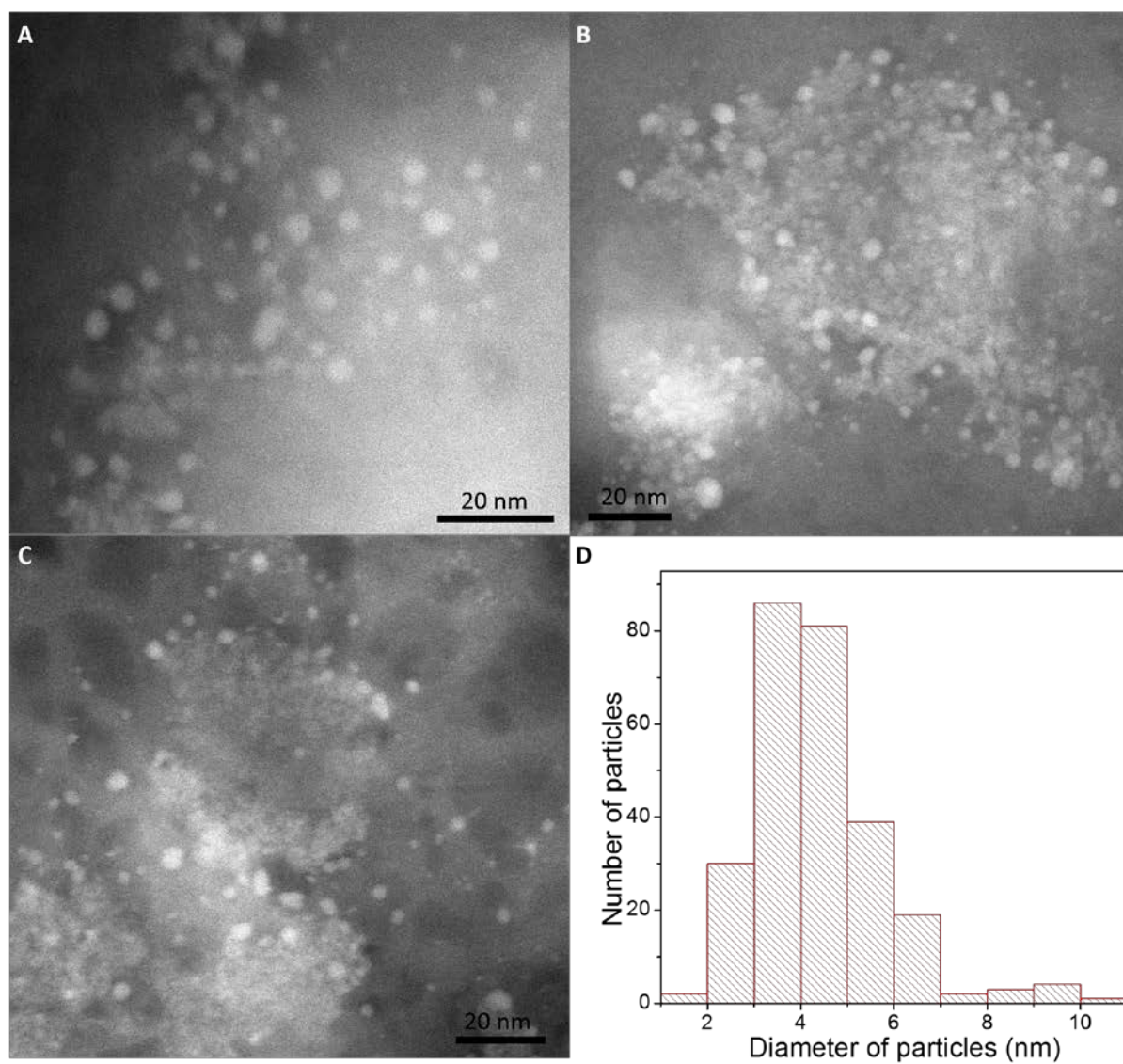
Fig. S2. (A-C) HAADF images of reduced Cu nanoparticles on MgO-Al$_2$O$_3$ support. (D) Size distribution of Cu nanoparticles.
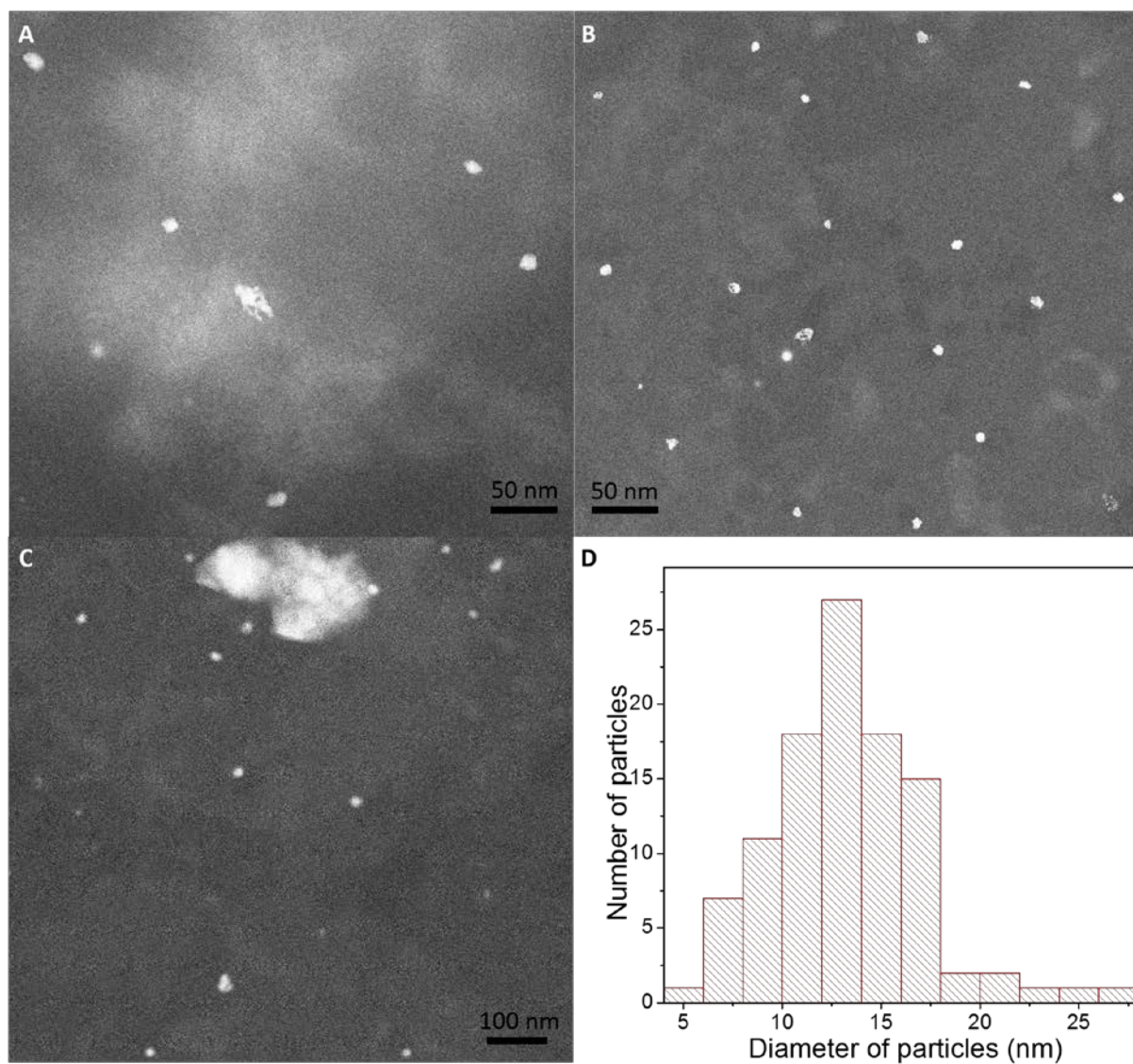
Fig. S3. (A-C) HAADF images of reduced Ru nanoparticles on MgO-Al$_2$O$_3$ support. (D) Size distribution of Ru nanoparticles.
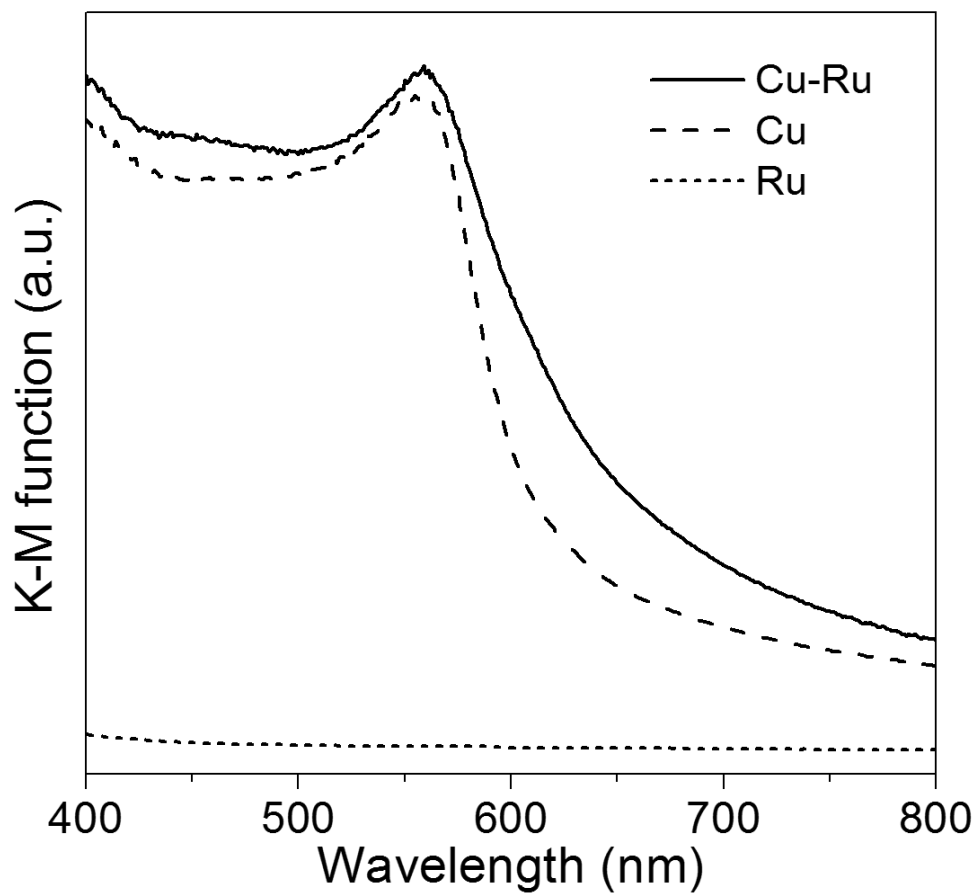
Fig. S4. UV-Vis diffuse reflectance spectra of Cu-Ru surface alloy (solid line), Cu nanoparticles (dashed line) and Ru nanoparticles (short-dashed line). Vertical axis is the Kubelka–Munk function.
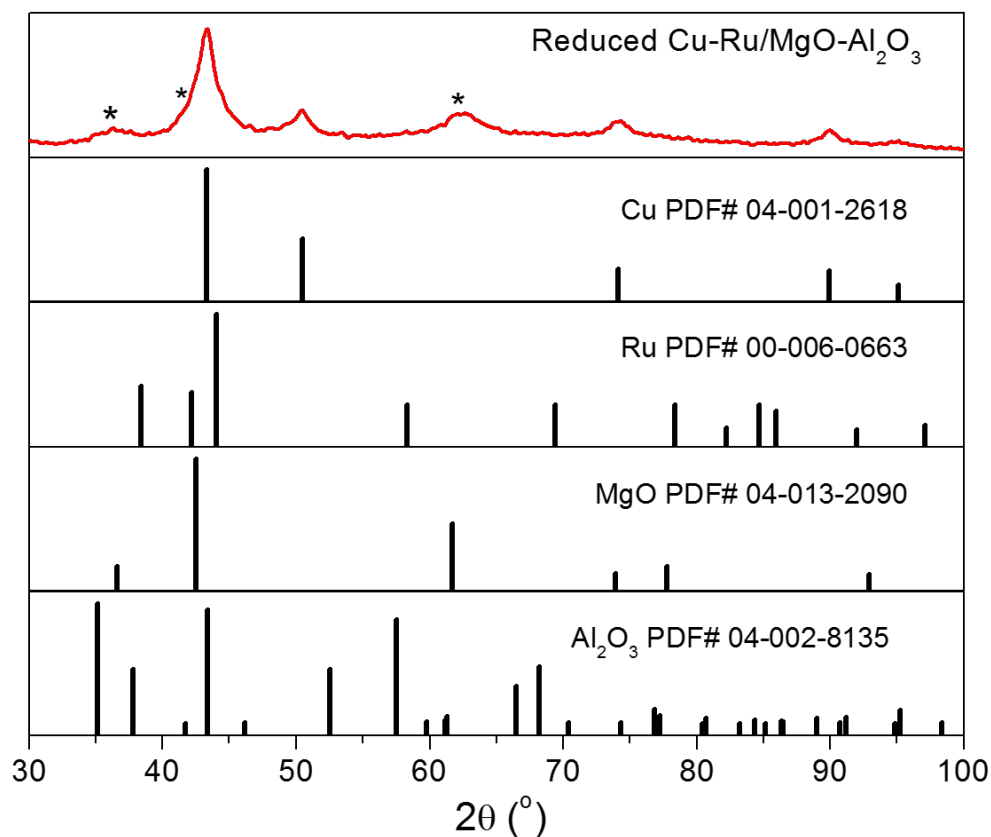
Fig. S5. Powder X-ray diffraction (PXRD) spectrum of Cu-Ru surface alloy on MgO-Al$_2$O$_3$ support and XRD data of Cu, Ru, MgO and Al$_2$O$_3$ from International Centre for Diffraction Data (ICDD) cards. The spectrum shows five peaks corresponding to metallic copper and three peaks/shoulder (labeled with *) matching with (111), (200), (220) of MgO. No peak corresponding to crystalline Al$_2$O$_3$ is found, indicating its amorphous structure. There is no peak corresponding to Ru either because of the low loading of Ru.
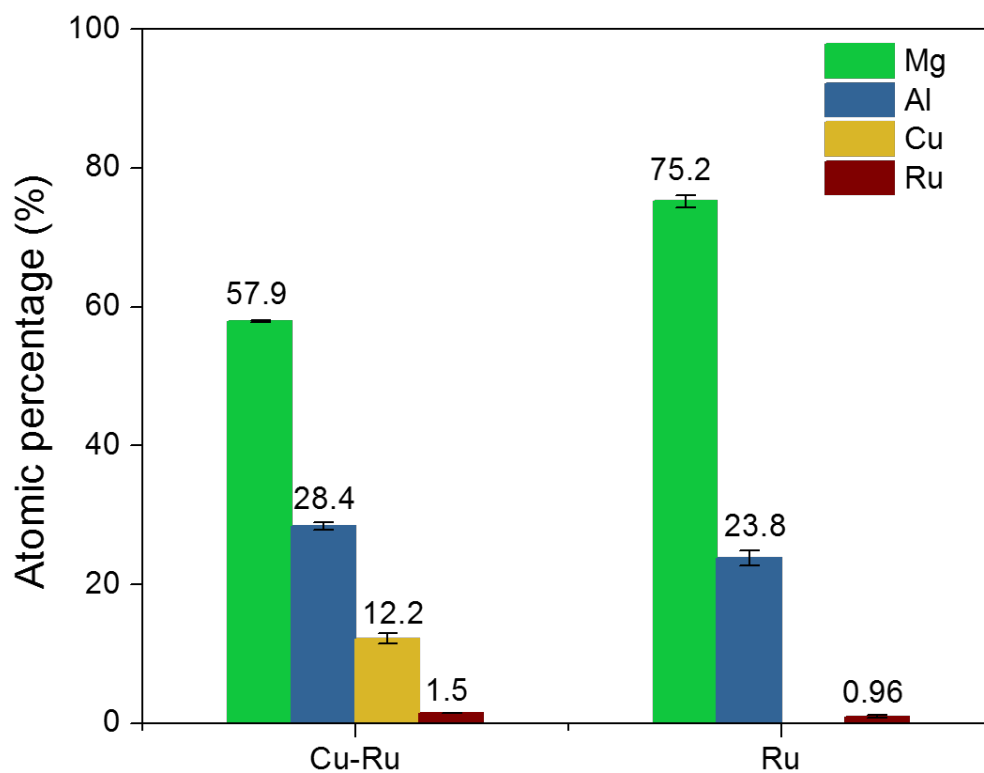
Fig. S6. XPS result of Cu-Ru surface alloy and Ru nanoparticles. Higher surface atomic percentage of ruthenium in Cu-Ru surface alloy also supports the proposed surface alloy structure.
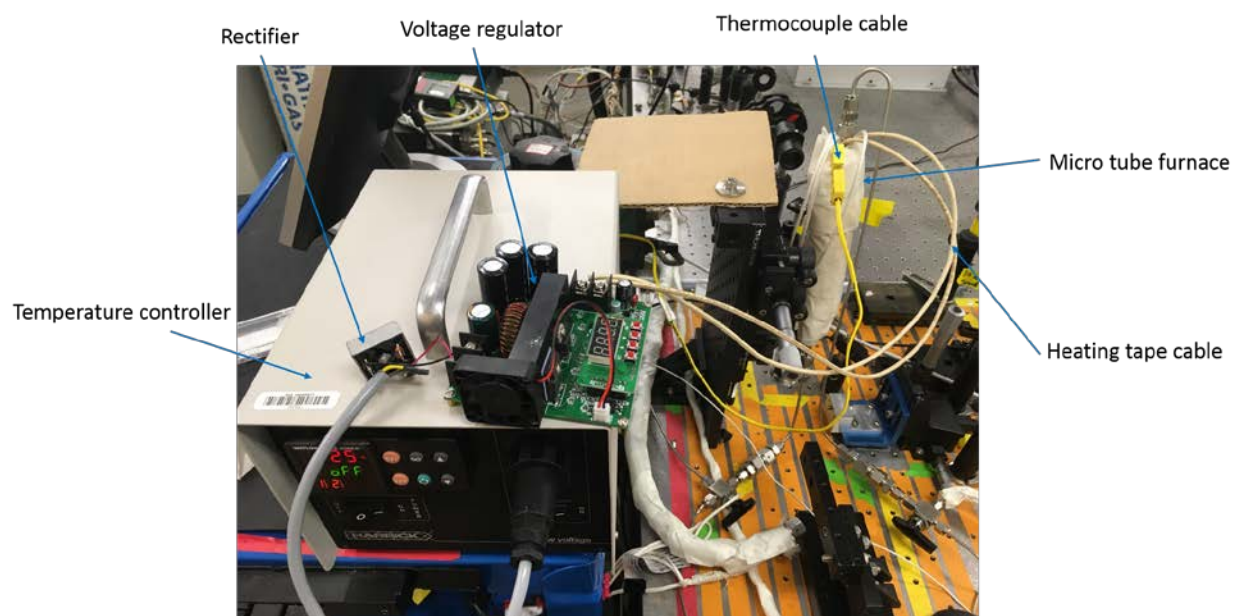
Fig. S7. Image of custom N_2O chemisorption setup.
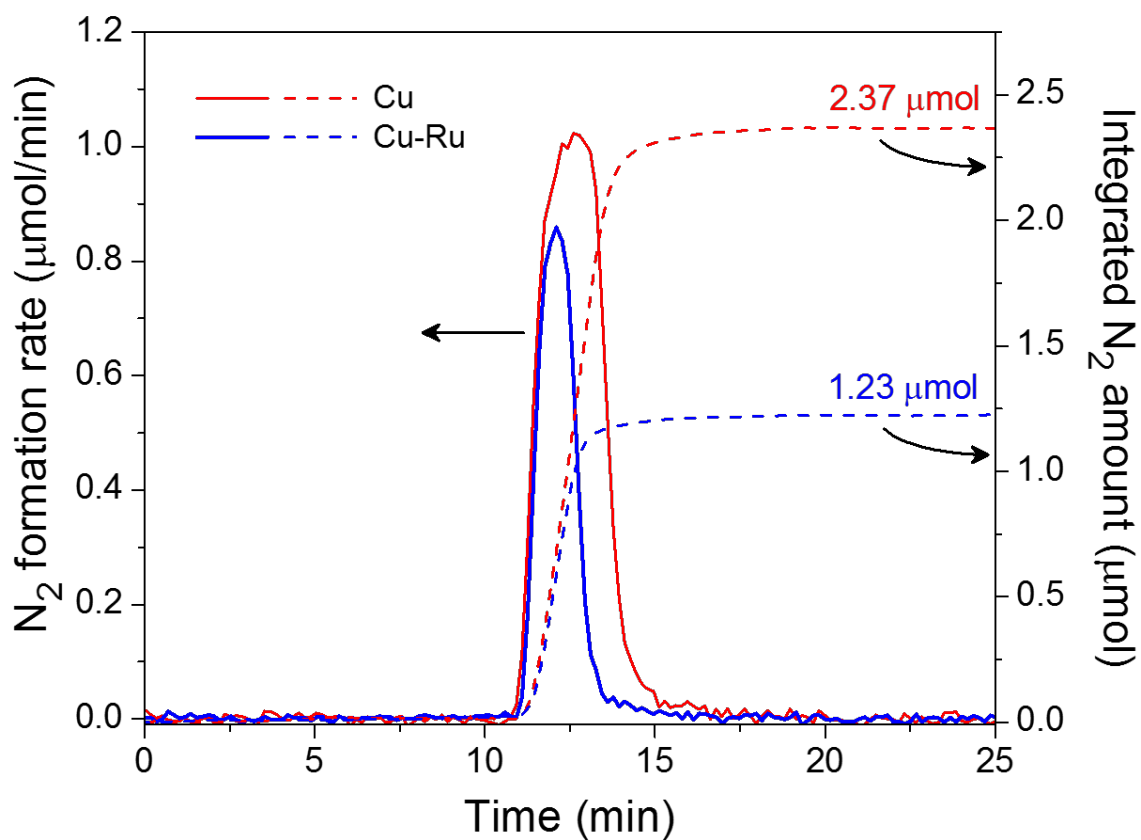
Fig. S8. N_2O chemisorption spectra of 50 mg Cu-Ru surface alloy (blue) and 50 mg Cu nanoparticles (red) at 40 ˚C. Solid lines show the N_2 formation rates, while dash lines represent the total amount of release N_2 by integrating the formation rate of N_2 over time.
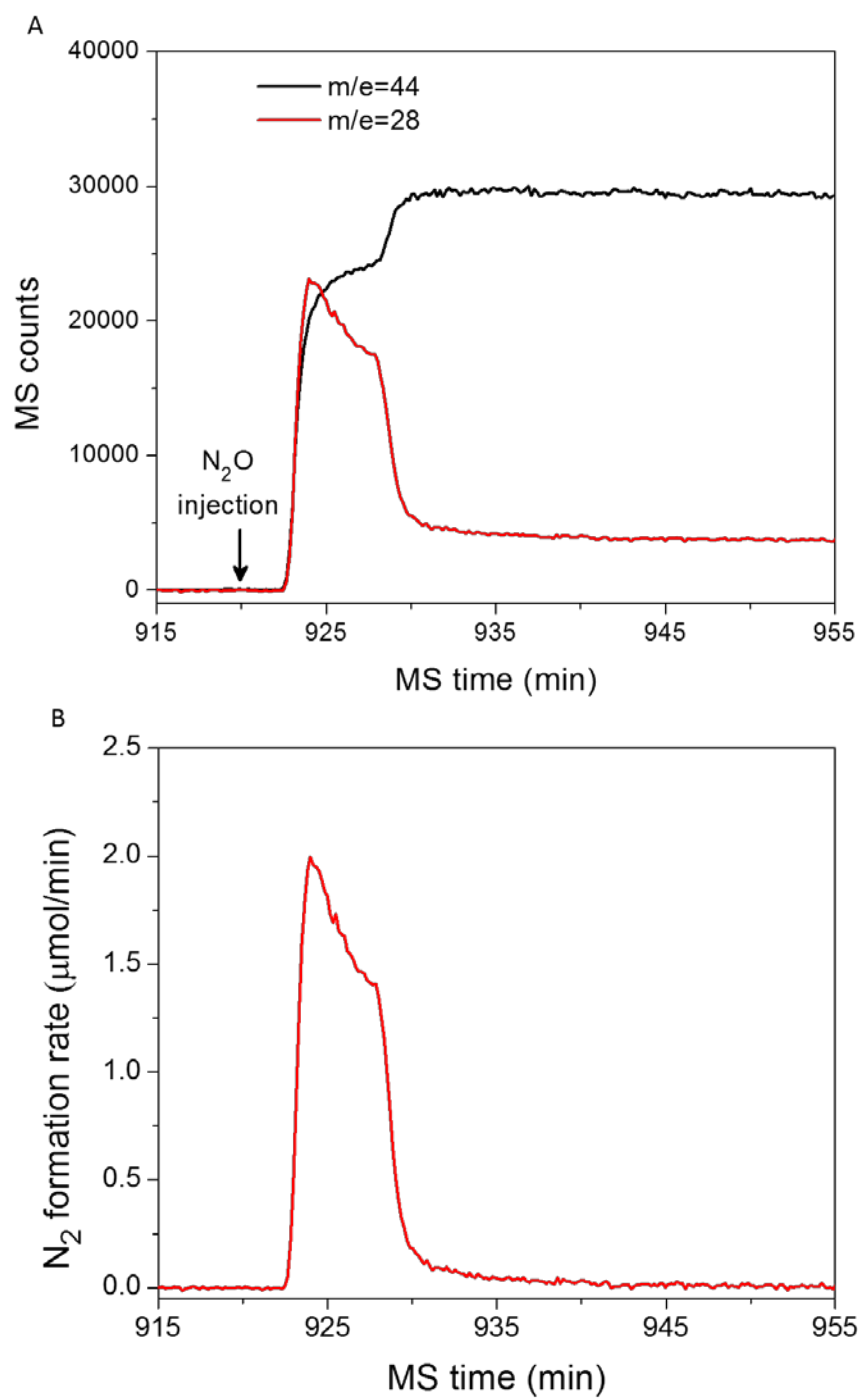
Fig. S9. (A) Raw mass spectra of m/e=28 and m/e=44 in N_2O chemisorption experiment of 0.1872g (after reduction) commercial copper nanoparticles powder at 40 ˚C. (B) Formation rate of N_2 obtained from data analysis of (A). Integration of the peak gives the total amount of released N_2 as 10.14 μmol and the corresponding specific surface concentration of copper is thus 108.3 μmol/g
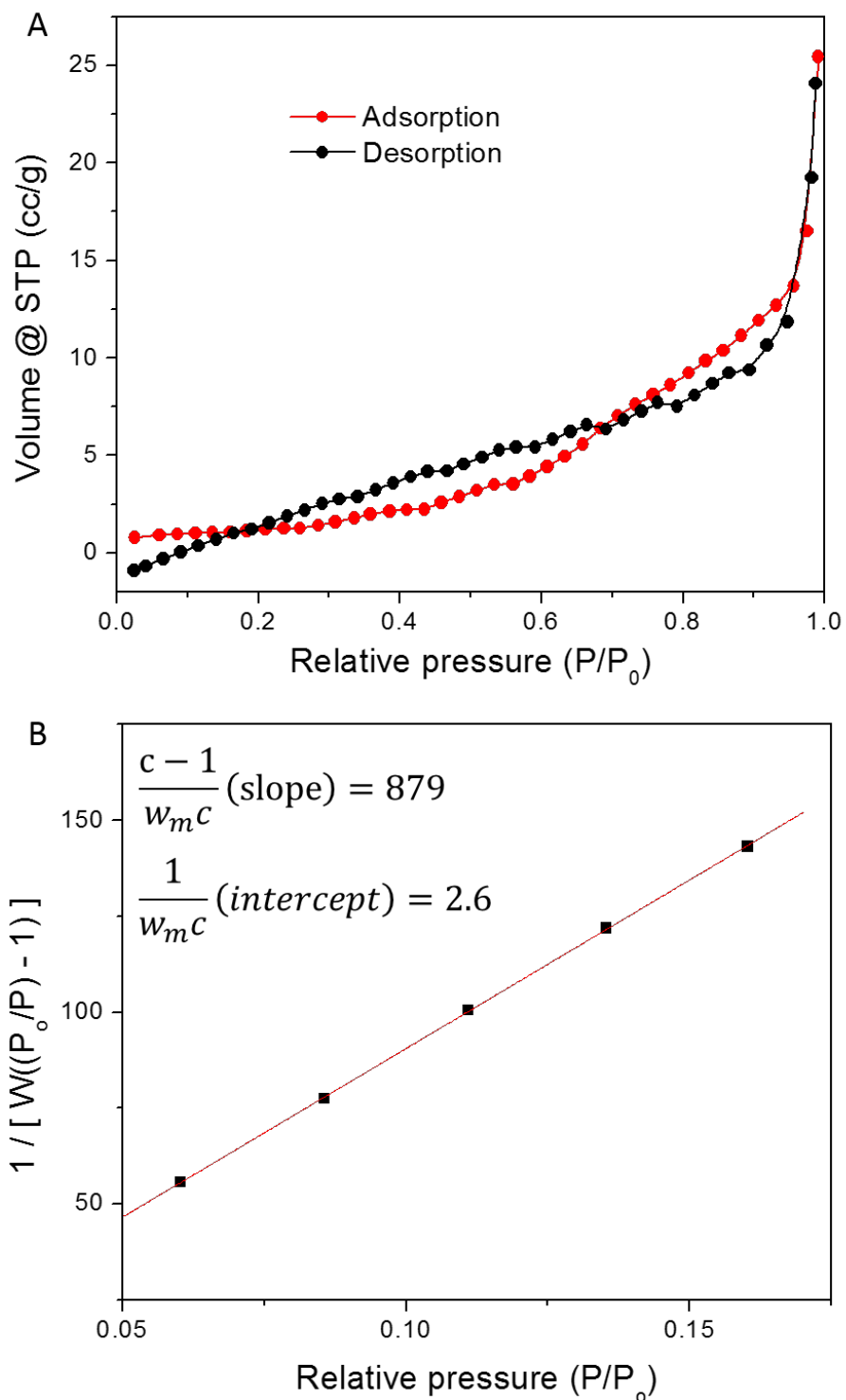
Fig. S10. (A) Nitrogen absorption-desorption isotherms of commercial copper nanoparticles powder at 77.35K. (B) BET surface area fitting of commercial copper nanoparticles powder. Surface area is 3.95 m^2/g and the specific surface concentration of copper is calculated to be 109.5 µmol/g.
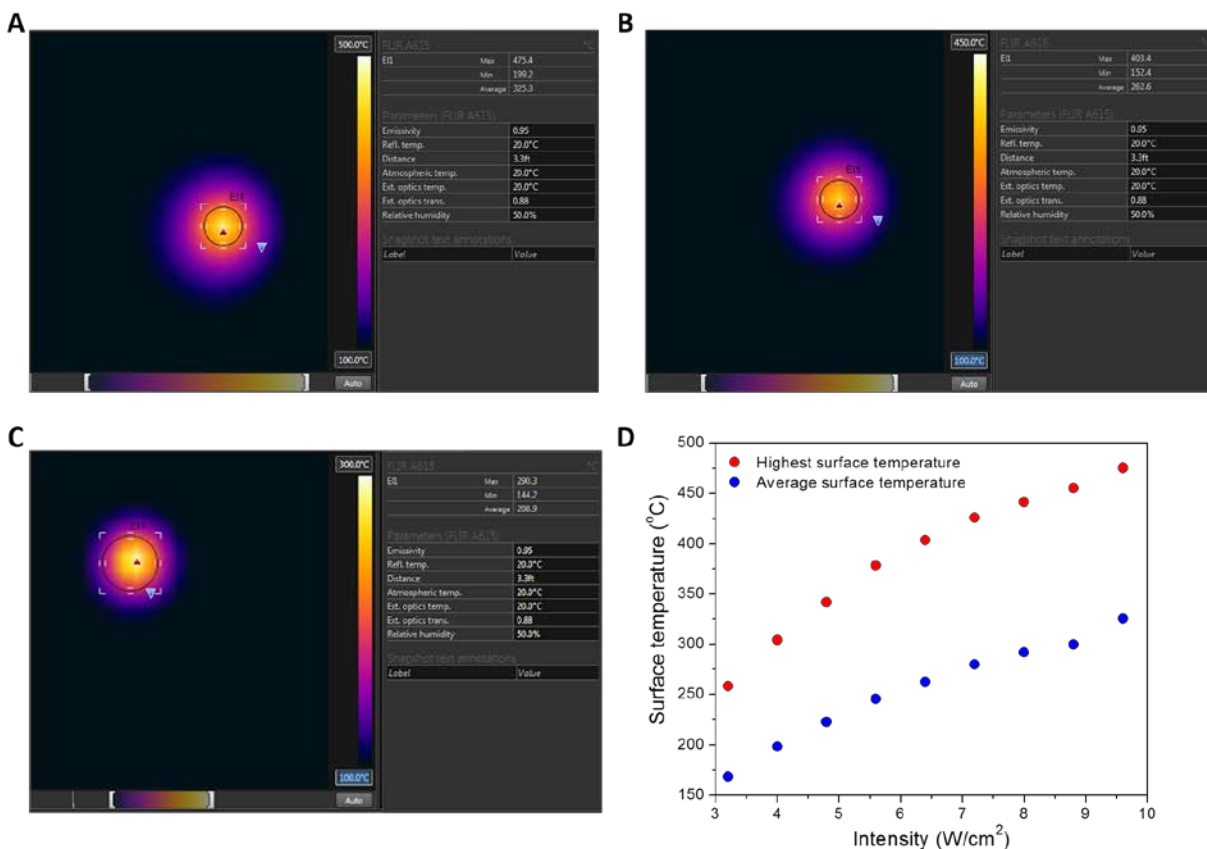
Fig. S11. Images of surface temperatures of sample pellet under (A) 9.6 W/cm^2 white light illumination; (B) 6.4 W/cm^2 white light illumination; (C) 3.2 W/cm^2 550 nm light illumination; all without external heating. (D) Plot of highest surface temperatures and average surface temperatures of sample pellet under white light illumination as a function of light intensity. The reactor temperature was kept at room temperature for the data presented here. Reasons for the nonlinear behavior in 11D include the temperature-dependent thermal conductivity of the support and the non-linear temperature dependence of the thermal radiative power.
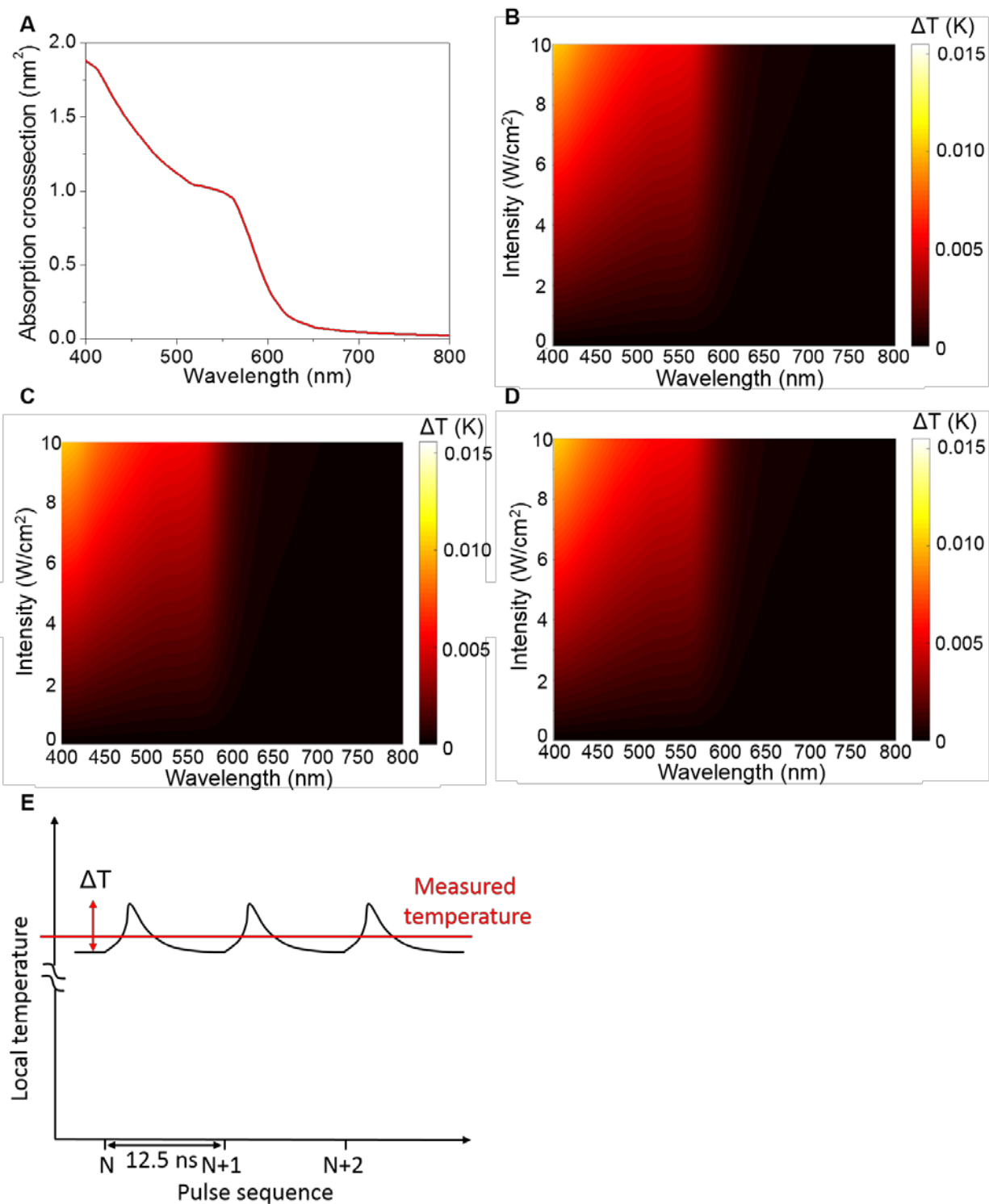
Fig. S12. (A) Simulated absorption cross-section spectrum of 5 nm copper nanoparticle based on Mie theory. (B-D) Contour map of calculated local temperature increase of 3 nm (B), 5 nm (C) and 10 nm (D) copper nanoparticle for different wavelengths and intensities. (E) Schematics of temporal local temperature of copper nanoparticles under illumination of periodic pulses.
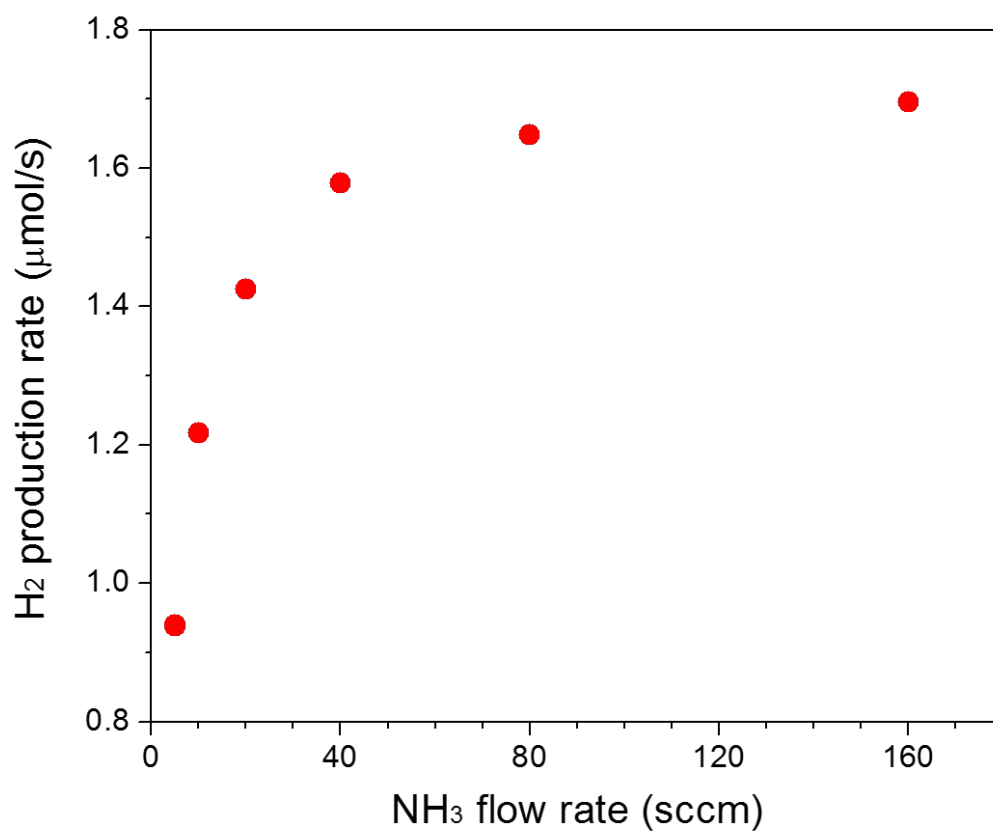
Fig. S13. NH$_3$-flow-rate dependence of photocatalytic reaction rate on Cu-Ru surface alloy under 9.6 W/cm^2 white light illumination. Flow rate above 80 sccm, corresponding to conversion below 2%, is needed to achieve differential reactor conditions in photocatalysis.
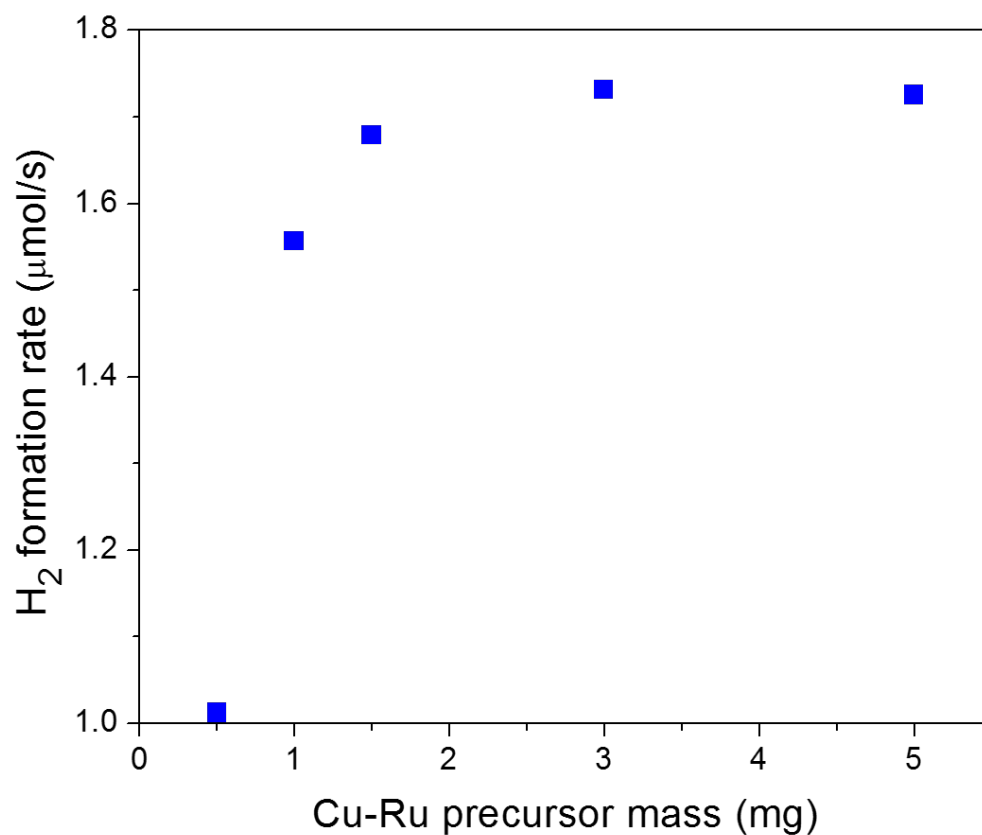
Fig. S14. Effect of loading amount of Cu-Ru surface alloy precursor on photocatalytic reaction rate under 9.6 W/cm^2 while light illumination and 100 sccm NH_3 flow rate. Around 1.5 mg photocatalyst precursor is needed to adsorb most of the light.
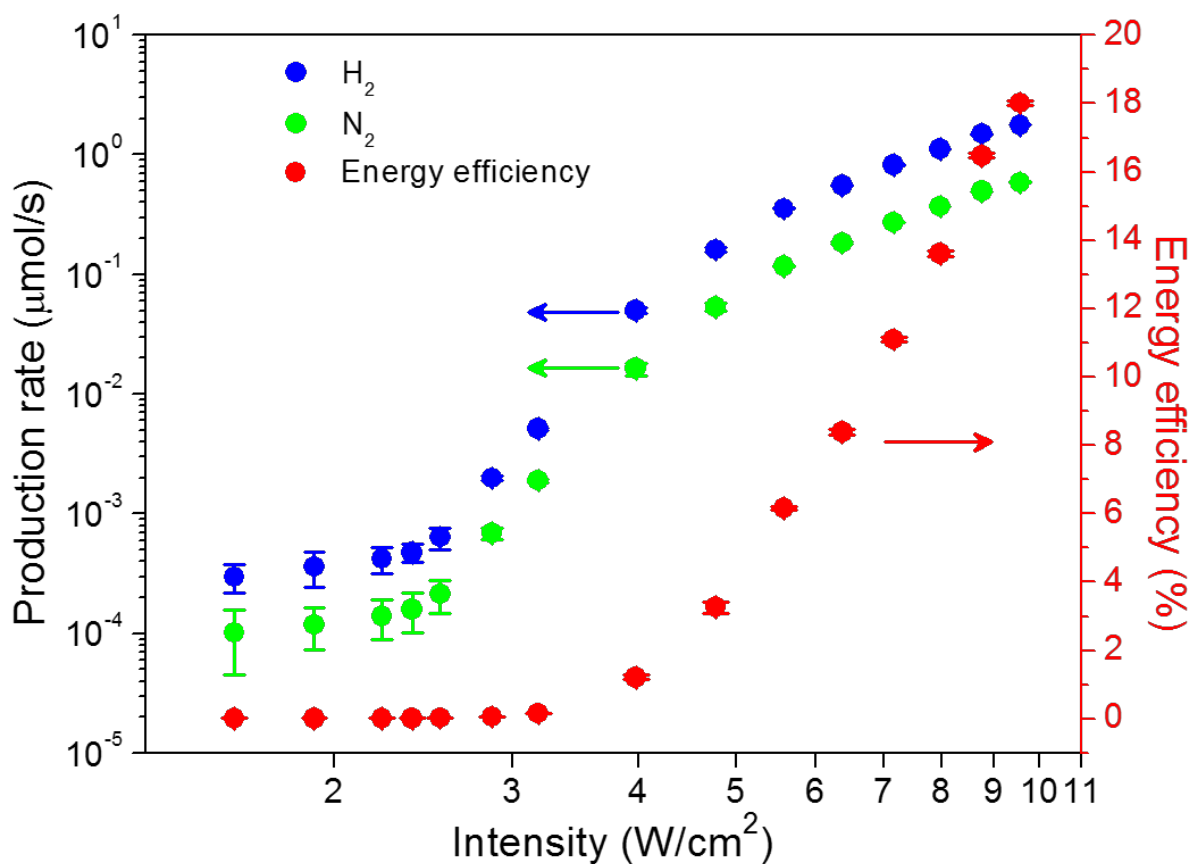
Fig. S15. Intensity dependence of photocatalytic reaction rate on Cu-Ru surface alloy. Feeding rate of NH_3 was 5 sccm for the intensity range of 1.6-3.2 W/cm^2 and 100 sccm for 4-9.6 W/cm^2 and 1.5 mg photocatalyst was used.
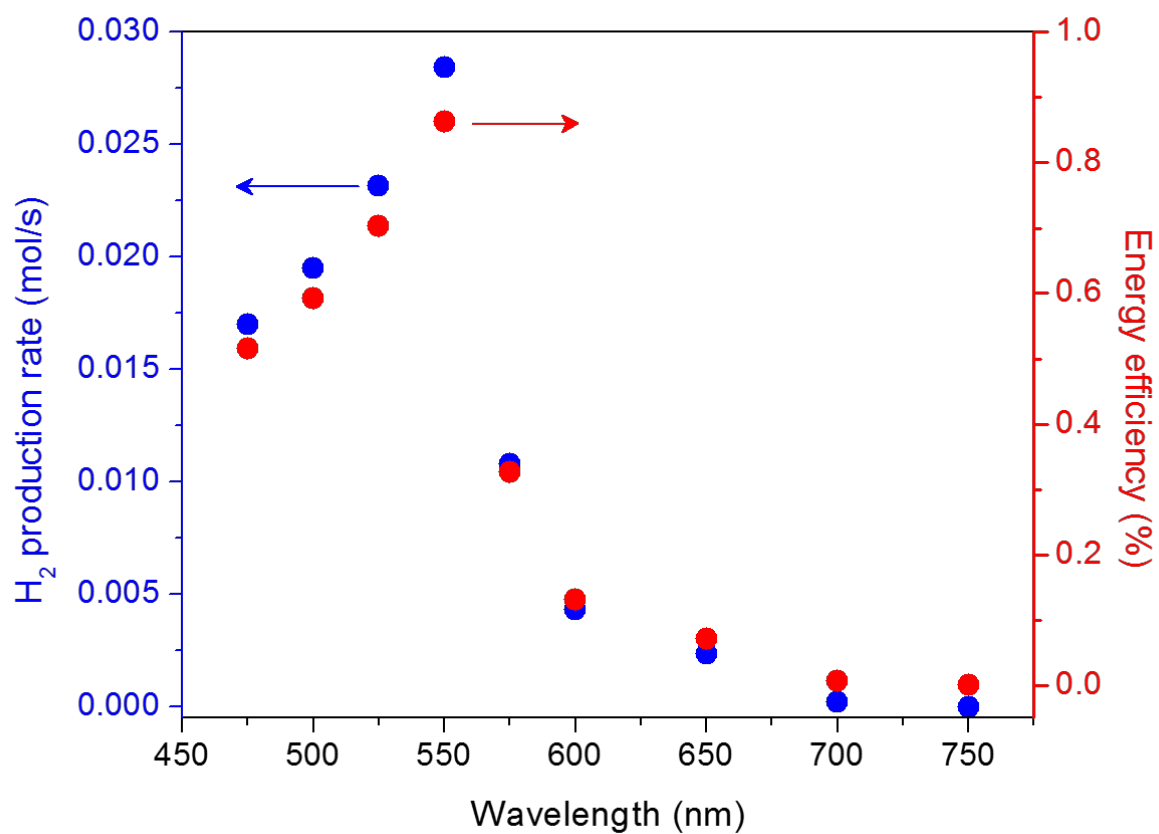
Fig. S16. Wavelength dependence of photocatalytic reaction rate on Cu-Ru surface alloy. Feeding rate of NH_3 was 5 sccm and 1.5 mg photocatalyst was used.
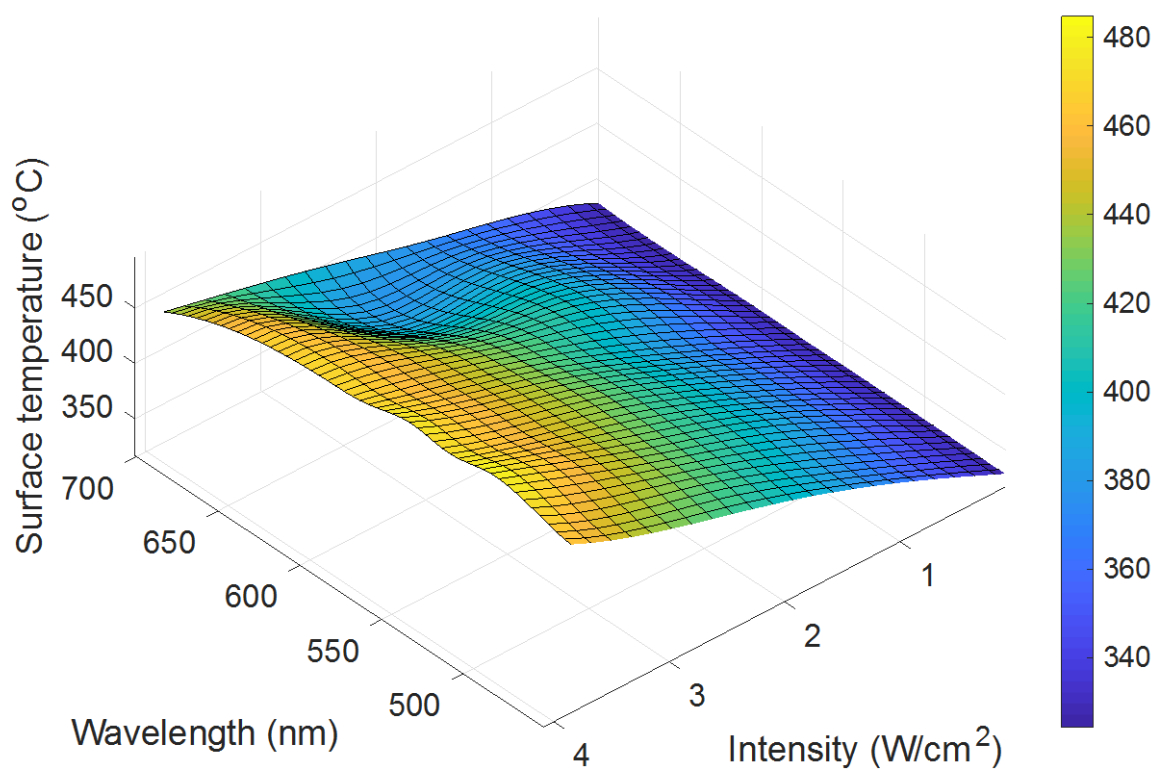
Fig. S17. 3D plot of wavelength- and intensity- dependence of surface temperature of catalyst pellet at chamber temperature of 377 ℃. Flow rate of NH₃ was 5 sccm.

Table S1. Element concentration in precursor from ICP

Sample	Metal element concentration (mmol/g precursor)	
	Cu	Ru
Cu-Ru	1.79	0.0565
Cu	1.94	N/A
Ru	N/A	0.0538

Table S2 Apparent activation barriers (eV) of various illumination conditions

Wavelength (nm)	Intensity (W/cm^2)				
	0.8	1.6	2.4	3.2	4
450	0.99	0.83	0.73	0.62	0.48
475	0.94	0.82	0.62	0.52	0.42
500	0.88	0.81	0.57	0.47	0.39
525	0.84	0.75	0.54	0.43	0.35
550	0.78	0.68	0.47	0.35	0.27
575	0.88	0.81	0.68	0.52	0.46
600	1.10	0.97	0.83	0.53	0.48
650	1.13	1.00	0.84	0.78	0.66
700	1.15	1.02	0.92	0.87	0.79

References and Notes

1. Y. Zhang, S. He, W. Guo, Y. Hu, J. Huang, J. R. Mulcahy, W. D. Wei, Surface-plasmon-driven hot electron photochemistry. *Chem. Rev.* **118**, 2927–2954 (2017). doi:10.1021/acs.chemrev.7b00430 Medline

2. B. Y. Zheng, H. Zhao, A. Manjavacas, M. McClain, P. Nordlander, N. J. Halas, Distinguishing between plasmon-induced and photoexcited carriers in a device geometry. *Nat. Commun.* **6**, 7797 (2015). doi:10.1038/ncomms8797 Medline

3. C. Zhang, H. Zhao, L. Zhou, A. E. Schlather, L. Dong, M. J. McClain, D. F. Swearer, P. Nordlander, N. J. Halas, Al-Pd nanodisk heterodimers as antenna-reactor photocatalysts. *Nano Lett.* **16**, 6677–6682 (2016). doi:10.1021/acs.nanolett.6b03582 Medline

4. D. F. Swearer, H. Zhao, L. Zhou, C. Zhang, H. Robatjazi, J. M. P. Martirez, C. M. Krauter, S. Yazdi, M. J. McClain, E. Ringe, E. A. Carter, P. Nordlander, N. J. Halas, Heterometallic antenna-reactor complexes for photocatalysis. *Proc. Natl. Acad. Sci. U.S.A.* **113**, 8916–8920 (2016). doi:10.1073/pnas.1609769113 Medline

5. P. Christopher, H. Xin, A. Marimuthu, S. Linic, Singular characteristics and unique chemical bond activation mechanisms of photocatalytic reactions on plasmonic nanostructures. *Nat. Mater.* **11**, 1044–1050 (2012). doi:10.1038/nmat3454 Medline

6. X. Zhang, X. Li, M. E. Reish, D. Zhang, N. Q. Su, Y. Gutiérrez, F. Moreno, W. Yang, H. O. Everitt, J. Liu, Plasmon-enhanced catalysis: Distinguishing thermal and nonthermal effects. *Nano Lett.* **18**, 1714–1723 (2018). doi:10.1021/acs.nanolett.7b04776 Medline

7. Y. Yu, V. Sundaresan, K. A. Willets, Hot carriers versus thermal effects: Resolving the enhancement mechanisms for plasmon-mediated photoelectrochemical reactions. *J. Phys. Chem. C* **122**, 5040–5048 (2018). doi:10.1021/acs.jpcc.7b12080

8. X. Zhang, X. Li, D. Zhang, N. Q. Su, W. Yang, H. O. Everitt, J. Liu, Product selectivity in plasmonic photocatalysis for carbon dioxide hydrogenation. *Nat. Commun.* **8**, 14542 (2017). doi:10.1038/ncomms14542 Medline

9. H. Song, X. Meng, T. D. Dao, W. Zhou, H. Liu, L. Shi, H. Zhang, T. Nagao, T. Kako, J. Ye, Light-enhanced carbon dioxide activation and conversion by effective plasmonic coupling effect of Pt and Au nanoparticles. *ACS Appl. Mater. Interfaces* **10**, 408–416 (2018). doi:10.1021/acsami.7b13043 Medline

10. Y. Kim, D. Dumett Torres, P. K. Jain, Activation energies of plasmonic catalysts. *Nano Lett.* **16**, 3399–3407 (2016). doi:10.1021/acs.nanolett.6b01373 Medline

11. G. Ertl, M. Huber, Mechanism and kinetics of ammonia decomposition on iron. *J. Catal.* **61**, 537–539 (1980). doi:10.1016/0021-9517(80)90403-0

12. M. C. J. Bradford, P. E. Fanning, M. A. Vannice, Kinetics of NH_3 decomposition over well dispersed Ru. *J. Catal.* **172**, 479–484 (1997). doi:10.1006/jcat.1997.1877

13. T. E. Bell, L. Torrente-Murciano, H_2 production via ammonia decomposition using non-noble metal catalysts: A review. *Top. Catal.* **59**, 1438–1457 (2016). doi:10.1007/s11244-016-0653-4

14. F. Schüth, R. Palkovits, R. Schlögl, D. S. Su, Ammonia as a possible element in an energy infrastructure: Catalysts for ammonia decomposition. *Energy Environ. Sci.* **5**, 6278–6289 (2012). doi:10.1039/C2EE02865D

15. A. Amano, H. Taylor, The decomposition of ammonia on ruthenium, rhodium and palladium catalysts supported on alumina. *J. Am. Chem. Soc.* **76**, 4201–4204 (1954). doi:10.1021/ja01645a057

16. M. Behrens, Coprecipitation: An excellent tool for the synthesis of supported metal catalysts—From the understanding of the well known recipes to new materials. *Catal. Today* **246**, 46–54 (2015). doi:10.1016/j.cattod.2014.07.050

17. H. Robatjazi, H. Zhao, D. F. Swearer, N. J. Hogan, L. Zhou, A. Alabastri, M. J. McClain, P. Nordlander, N. J. Halas, Plasmon-induced selective carbon dioxide conversion on earth-abundant aluminum-cuprous oxide antenna-reactor nanoparticles. *Nat. Commun.* **8**, 27 (2017). doi:10.1038/s41467-017-00055-z Medline

18. V. K. Pustovalov, Theoretical study of heating of spherical nanoparticle in media by short laser pulses. *Chem. Phys.* **308**, 103–108 (2005). doi:10.1016/j.chemphys.2004.08.005

19. A. M. Goodman, N. J. Hogan, S. Gottheim, C. Li, S. E. Clare, N. J. Halas, Understanding resonant light-triggered DNA release from plasmonic nanoparticles. *ACS Nano* **11**, 171–179 (2017). doi:10.1021/acsnano.6b06510 Medline

20. S. C. Nguyen, Q. Zhang, K. Manthiram, X. Ye, J. P. Lomont, C. B. Harris, H. Weller, A. P. Alivisatos, Study of heat transfer dynamics from gold nanorods to the environment via time-resolved infrared spectroscopy. *ACS Nano* **10**, 2144–2151 (2016). doi:10.1021/acsnano.5b06623 Medline

21. G. H. Chan, J. Zhao, E. M. Hicks, G. C. Schatz, R. P. Van Duyne, Plasmonic properties of copper nanoparticles fabricated by nanosphere lithography. *Nano Lett.* **7**, 1947–1952 (2007). doi:10.1021/nl070648a

22. J. Zhao, S. C. Nguyen, R. Ye, B. Ye, H. Weller, G. A. Somorjai, A. P. Alivisatos, F. D. Toste, A comparison of photocatalytic activities of gold nanoparticles following plasmonic and interband excitation and a strategy for harnessing interband hot carriers for solution phase photocatalysis. *ACS Cent. Sci.* **3**, 482–488 (2017). doi:10.1021/acscentsci.7b00122 Medline

23. H. I. Villafán-Vidales, S. Abanades, C. Caliot, H. Romero-Paredes, Heat transfer simulation in a thermochemical solar reactor based on a volumetric porous receiver. *Appl. Therm. Eng.* **31**, 3377–3386 (2011). doi:10.1016/j.applthermaleng.2011.06.022

24. F. J. Valdés-Parada, H. Romero-Paredes, G. Espinosa-Paredes, Numerical simulation of a tubular solar reactor for methane cracking. *Int. J. Hydrogen Energy* **36**, 3354–3363 (2011). doi:10.1016/j.ijhydene.2010.12.022

25. H. Lynggaard, A. Andreasen, C. Stegelmann, P. Stoltze, Analysis of simple kinetic models in heterogeneous catalysis. *Prog. Surf. Sci.* **77**, 71–137 (2004). doi:10.1016/j.progsurf.2004.09.001

26. W. Tsai, W. H. Weinberg, Steady-state decomposition of ammonia on the Ru(001) surface. *J. Phys. Chem.* **91**, 5302–5307 (1987). doi:10.1021/j100304a034

27. C. Egawa, T. Nishida, S. Naito, K. Tamaru, Ammonia decomposition on (1 1 10) and (0 0 1) surfaces of ruthenium. *J. Chem. Soc., Faraday Trans. I* **80**, 1595–1604 (1984). doi:10.1039/f19848001595

28. A. Hellman, K. Honkala, I. N. Remediakis, Á. Logadóttir, A. Carlsson, S. Dahl, C. H. Christensen, J. K. Nørskov, Ammonia synthesis and decomposition on a Ru-based catalyst modeled by first-principles. *Surf. Sci.* **603**, 1731–1739 (2009). doi:10.1016/j.susc.2008.10.059

29. V. Prasad, A. M. Karim, A. Arya, D. G. Vlachos, Assessment of overall rate expressions and multiscale, microkinetic model uniqueness via experimental data injection: Ammonia decomposition on Ru/γ-Al_2O_3 for hydrogen production. *Ind. Eng. Chem. Res.* **48**, 5255–5265 (2009). doi:10.1021/ie900144x

30. C. T. Campbell, The degree of rate control: A powerful tool for catalysis research. *ACS Catal.* **7**, 2770–2779 (2017). doi:10.1021/acscatal.7b00115

31. J. G. Liu, H. Zhang, S. Link, P. Nordlander, Relaxation of plasmon-induced hot carriers. *ACS Photonics* **5**, 2584–2595 (2017). doi:10.1021/acsphotonics.7b00881

32. P. R. Shirhatti, I. Rahinov, K. Golibrzuch, J. Werdecker, J. Geweke, J. Altschäffel, S. Kumar, D. J. Auerbach, C. Bartels, A. M. Wodtke, Observation of the adsorption and desorption of vibrationally excited molecules on a metal surface. *Nat. Chem.* **10**, 592–598 (2018). doi:10.1038/s41557-018-0003-1 Medline

33. H. L. Dai, W. Ho, *Laser Spectroscopy and Photochemistry on Metal Surfaces* (World Scientific, 1995).

34. C. Frischkorn, M. Wolf, Femtochemistry at metal surfaces: Nonadiabatic reaction dynamics. *Chem. Rev.* **106**, 4207–4233 (2006). doi:10.1021/cr050161r Medline

35. S. A. Buntin, L. J. Richter, R. R. Cavanagh, D. S. King, Optically driven surface reactions: Evidence for the role of hot electrons. *Phys. Rev. Lett.* **61**, 1321–1324 (1988). doi:10.1103/PhysRevLett.61.1321 Medline

36. V. A. Spata, E. A. Carter, Mechanistic insights into photocatalyzed hydrogen desorption from palladium surfaces assisted by localized surface plasmon resonances. *ACS Nano* **12**, 3512–3522 (2018). doi:10.1021/acsnano.8b00352 Medline

37. O. Hinrichsen, T. Genger, M. Muhler, Chemisorption of N_2O and H_2 for the surface determination of copper catalysts. *Chem. Eng. Technol.* **23**, 956–959 (2000). doi:10.1002/1521-4125(200011)23:11<956:AID-CEAT956>3.0.CO;2-L

38. J. J. F. Scholten, A. P. Pijpers, A. M. L. Hustings, Surface characterization of supported and nonsupported hydrogenation catalysts. *Catal. Rev., Sci. Eng.* **27**, 151–206 (1985). doi:10.1080/01614948509342359

39. H. Li, M. Rivallan, F. Thibault-Starzyk, A. Travert, F. C. Meunier, Effective bulk and surface temperatures of the catalyst bed of FT-IR cells used for in situ and operando studies. *Phys. Chem. Chem. Phys.* **15**, 7321–7327 (2013). doi:10.1039/c3cp50442e Medline

40. C. F. Bohren, E. E. Clothiaux, D. R. Huffman, *Absorption and Scattering of Light by Small Particles* (Wiley-VCH, 2009).

41. E. D. Palik, G. Ghosh, *Handbook of Optical Constants of Solids Five-Volume Set* (Academic Press, 1998).

42. T. C. Choy, *Effective Medium Theory: Principles and Applications* (Oxford Univ. Press, 2016).

43. G. Baffou, H. Rigneault, Femtosecond-pulsed optical heating of gold nanoparticles. *Phys. Rev. B* **84**, 035415 (2011). doi:10.1103/PhysRevB.84.035415

44. H. Mortensen, L. Diekhöner, A. Baurichter, E. Jensen, A. C. Luntz, Dynamics of ammonia decomposition on Ru(0001). *J. Chem. Phys.* **113**, 6882–6887 (2000). doi:10.1063/1.1310662